SLAC-PUB-12839
arXiv:0709.1528[astro-ph]
September 2007

Multiwavelength Observations of the Powerful γ-ray Quasar PKS 1510−089: Clues on the Jet Composition

J. Kataoka[1], G. Madejski[2], M. Sikora[3], P. Roming[4], M. M. Chester[4], D. Grupe[4], Y. Tsubuku[1], R. Sato[1], N. Kawai[1], G. Tosti[5], D. Impiombato[5], Y. Y. Kovalev[6,7], Y. A. Kovalev[7], P. G. Edwards[8], S. J. Wagner[9], R. Moderski[3], Ł. Stawarz[2,10], T. Takahashi[11], and S. Watanabe[11],

ABSTRACT

We present the results from a multiwavelength campaign conducted in August 2006 of the powerful γ-ray quasar PKS 1510−089 ($z = 0.361$). This campaign commenced with a deep *Suzaku* observation lasting three days for a total exposure time of 120 ks, and continued with *Swift* monitoring over 18 days. Besides *Swift* observations, which sampled the optical/UV flux in all 6 UVOT filters as well as the X-ray spectrum in the 0.3−10 keV energy range, the campaign included ground-based optical and radio data, and yielded a quasi-simultaneous broad-band spectral energy distribution from 10^9 Hz to 10^{19} Hz. Thanks to its low instrumental background, the *Suzaku* observation provided a high S/N X-ray spectrum, which is well represented by an extremely hard power-law with photon index $\Gamma \simeq 1.2$, augmented by a soft component apparent below 1 keV, which is well described by a black-body model with temperature $kT \simeq 0.2$ keV. Monitoring by *Suzaku* revealed temporal variability which is different between the low and high energy bands, again suggesting the presence of a second, variable component in addition to

[1]Department of Physics, Tokyo Institute of Technology, Meguro, Tokyo, 152-8551, Japan

[2]Stanford Linear Accelerator Center and Kavli Institute for Particle Astrophysics and Cosmology, Stanford University, Stanford, CA 94305, USA

[3]Nicolaus Copernicus Astronomical Center, Bartycka 18, 00-716, Warsaw, Poland

[4]Department of Astronomy and Astrophysics, Pennsylvania State University, PA, 16802, USA

[5]Physics Department and Astronomical Observatory, University of Perugia, Perugia, Italy

[6]Max-Planck-Institut für Radioastronomie, Auf dem Hügel 69, 53121 Bonn, Germany

[7]Astro Space Center of the Lebedev Physical Institute, Profsoyuznaya 84/32, Moscow, 117997, Russia

[8]Australia Telescope National Facility, CSIRO, Locked Bag 194, Narrabri NSW 2390, Australia

[9]Landessternwarte Heidelberg, Kőnigstuhl, D-69117 Heidelberg, Germany

[10]Astronomical Observatory of the Jagiellonian University, ul. Orla 171, 30-244 Kraków, Poland

[11]Department of High Energy Astrophysics, ISAS, JAXA, Kanagawa, 229-8510, JAPAN

Submitted to Astrophysical Journal

Work supported in part by US Department of Energy contract DE-AC02-76SF00515

the primary power-law emission. We model the broadband spectrum of PKS 1510−089 assuming that the high energy spectral component results from Comptonization of infrared radiation produced by hot dust located in the surrounding molecular torus. In the adopted internal shock scenario, the derived model parameters imply that the power of the jet is dominated by protons but with a number of electrons/positrons exceeding a number of protons by a factor ~ 10. We also find that inhomogeneities responsible for the shock formation, prior to the collision may produce bulk-Compton radiation which can explain the observed soft X-ray excess and possible excess at ~ 18 keV. We note, however, that the bulk-Compton interpretation is not unique, and the observed soft excess could arise as well via some other processes discussed briefly in the text.

Subject headings: galaxies: active – galaxies: jets – (galaxies:) quasars: individual (PKS 1510−089) – X-rays: galaxies

1. Introduction

Powerful, highly-collimated outflows called jets are commonly observed in a wide variety of astronomical sources; for active galactic nuclei (AGNs; e.g., Urry & Padovani 1995), γ-ray bursts (e.g., Piran 2000), and binaries containing compact stars (e.g., Mirabel & Rodriguez 1999) we have excellent evidence that these outflows move with relativistic speeds. It has been a long-standing mystery, however, where and how the relativistic jets are formed, and what is their composition. From a theoretical standpoint, the relativistic AGN jets considered here can be launched as outflows dominated by Poynting flux generated in the force-free magnetospheres of black holes, or as hydromagnetic winds driven centrifugally from accretion discs (see review by Lovelace, Ustyugova, & Koldova 1999). In either case, strong magnetic fields are involved in driving the outflows, although many (if not most) observations indicate that eventually, *particles* carry the bulk of the jet's energy (Wardle et al. 1998; Sikora & Madejski 2000; Hirotani 2005; Sikora et al. 2005). This apparent discrepancy, however, can be resolved if the jets are indeed initially dominated by the Poynting flux but are efficiently converted into matter-dominated form at some later stage, most likely prior to the so-called "blazar zone" (see Sikora et al. 2005 and references therein). Such a "blazar zone," the region where the bulk of the observed nonthermal radiation is produced, is most likely located at $r \simeq 10^3{-}10^4\ r_g$, where $r_g = GM/c^2$ is the gravitational radius (Spada et al. 2000; Kataoka et al. 2001; Tanihata et al. 2003).

Here we adopt a scenario where a jet is launched near a rapidly rotating black hole, presumably at the innermost portions of the accretion disk (see, e.g., Koide et al. 1999). Such a jet, initially consisting of protons and electrons, is accelerated by large scale magnetic field stresses and within 100 r_g can be loaded by electron/positron ($e^- e^+$) pairs via interactions with the coronal soft γ-ray photons (note that such photons are directly seen in the spectra of Seyfert galaxies; see, e.g., Zdziarski, Poutanen & Johnson 2000). Hence, it is possible that relativistic jets in quasars (beyond

the jet formation zone) may well contain more electron/positron pairs than protons, but are still dynamically dominated by cold protons (Sikora et al. 1997; Sikora & Madejski 2000).

Observations with the EGRET instrument on board the *Compton Gamma-Ray Observatory* in the γ-ray band have opened a new window for studying AGN jets, and revealed that many radio-bright and variable AGN are also the brightest extragalactic MeV−GeV γ-ray emitters (see, e.g., Hartman et al. 1999). The properties of the γ-ray emission in those objects — often termed "blazars" — supported earlier inferences based on radio and optical data, and independently indicated significant Doppler boosting, implying the origin of broad-band emission in a compact, relativistic jet pointing close to our line of sight. Generally, the overall spectra of blazar sources (plotted in the $\log(\nu)$-$\log(\nu F_\nu)$ plane, where F_ν is the observed spectral flux energy density) have two pronounced continuum components: one peaking between IR and X-rays and the other in the γ-ray regime (see, e.g., Kubo et al. 1998; Ghisellini et al. 1998). The lower energy component is believed to be produced by the synchrotron radiation of relativistic electrons accelerated within the outflow, while inverse Compton (IC) emission by the same electrons is most likely responsible for the formation of the high energy γ-ray component. It is widely believed, in addition, that the IC emission from flat spectrum radio quasars (FSRQ) is dominated by the scattering of soft photons external to the jet (external Compton process, ERC), which are produced by the accretion disk, either directly or indirectly via scattering/reprocessing in the broad line region (BLR) or dusty torus (see, e.g., Dermer & Schlickeiser 1993; Sikora, Begelman, & Rees 1994). Other sources of seed photons can also contribute to the observed IC component, in particular the synchrotron photons themselves via the synchrotron self-Compton process (SSC) which under certain conditions can even dominate the observed high energy radiation (Sokolov & Marscher 2005). Detailed modelling of broad-band blazar emission can provide information about the location of the dissipative regions in blazars, the energy distribution of relativistic electrons/positrons, the magnetic field intensity, and the jet power.

A probe of the low energy electron/positron content in blazars was proposed by Begelman & Sikora (1987), and extensively studied in the literature (Sikora & Madejski 2000; Moderski et al. 2004; Celotti et al. 2007)[1]. The γ-ray emission is produced by electrons/positrons accelerated *in situ*, and thus before reaching the blazar dissipative site the electrons/positrons are expected to be cold. If they are transported by a jet with a bulk Lorentz factor $\Gamma_{\rm jet} \geq 10$, they upscatter external UV photons up to X-ray energies and produce a relatively narrow feature expected to be located in the soft/mid X-ray band, with the flux level reflecting the amount of cold electrons and the jet velocity. Unfortunately, such an additional bulk-Compton (BC) spectral component is difficult to observe because of the presence of strong non-thermal blazar emission, which dilutes any other radiative signatures of the active nucleus. In this context, FSRQs may constitute a possible exception, since their non-thermal X-ray emission is relatively weak when compared to other types

[1]See also Georganopoulos et al. (2005) and Uchiyama et al. (2005) for applications of the bulk-Compton constraints on the parameters of AGN jets on large-scales.

of blazar sources.

PKS 1510−089 is a nearby ($z = 0.361$) highly polarized quasar (HPQ) detected in the MeV−GeV band by EGRET. It is a highly superluminal jet source, with apparent velocities of $v_{\rm app} \gtrsim 10\ c$ observed in multi-epoch VLBA observations (Homan et al. 2001; Wardle et al. 2005; Jorstad et al. 2005). Its broad-band spectrum is representative of other FSRQs. In particular, its radiative output is dominated by the γ-ray inverse-Compton component, while its synchrotron emission peaks around IR frequencies below the pronounced UV bump, which is in turn presumably due to the thermal emission from the accretion disk (Malkan & Moore 1986; Pian & Treves 1993). PKS 1510−089 has been extensively studied by X-ray satellites, especially *ROSAT* (Siebert et al. 1996), *ASCA* (Singh, Shrader, & George 1997), and *Chandra* (Gambill et al. 2003). The observed X-ray spectrum was very flat in the 2−10 keV band (photon index $\Gamma \simeq 1.3$), but steepened (to $\Gamma \simeq 1.9$) in the *ROSAT* bandpass (below 2 keV). Recent observations by *BeppoSAX* (Tavecchio et al. 2000) confirmed the presence of a soft X-ray excess below 1 keV. All these findings suggest that PKS 1510−089 may be among the best candidates for detecting the BC bump.

In this paper, we present a detailed analysis of 120 ks observations of PKS 1510−089 with *Suzaku* in August 2006 as a part of the AO-1 program, in addition to a long *Swift* XRT/UVOT monitoring campaign followed-up by ground-based optical and radio telescopes. Thanks to the good photon statistics and the low background of the *Suzaku*/*Swift* data, we successfully obtained the highest quality data on PKS 1510−089 ever reported, over ten decades in frequency, between 10^9 Hz and 10^{19} Hz. The observation and analysis methods are described in §2. Detailed spectral studies and temporal analysis are presented in §3. Based on these new findings, in §4 we discuss the nature of the observed spectral features. Finally, our main conclusions are given in §5. Throughout this paper we adopt a luminosity distance of $d_{\rm L} = 1919$ Mpc for PKS 1510−089 ($z = 0.361$), derived for a modern cosmology with $\Omega_{\rm m} = 0.27$, $\Omega_\Lambda = 0.73$ and $H_0 = 71\,{\rm km\,s^{-1}\,Mpc^{-1}}$.

2. Observations and Data Reduction

2.1. *Suzaku*

PKS 1510−089 was observed with *Suzaku* (Mitsuda et al. 2007) in August 2006 over approximately three days. Table 1 summarizes the start and end times, and the exposures of the *Suzaku* observation (sequence number 701094010). *Suzaku* carries four sets of X-ray telescopes (Serlemitsos et al. 2007) each with a focal-plane X-ray CCD camera (XIS, X-ray Imaging Spectrometer; Koyama et al. 2007) that is sensitive in the energy range of 0.3−12 keV, together with a non-imaging Hard X-ray Detector (HXD; Takahashi et al. 2007; Kokubun et al. 2007), which covers the 10−600 keV energy band with Si PIN photo-diodes and GSO scintillation detectors. Three of the XIS (XIS 0, 2, 3) detectors have front-illuminated (FI) CCDs, while the XIS 1 utilizes a back-illuminated (BI) CCD. The merit of the BI CCD is its improved sensitivity in the soft X-ray energy band below 1 keV. PKS 1510−089 was focused on the nominal center position of the XIS detectors.

2.1.1. XIS Data Reduction

For the XIS, we analyzed the screened data, reduced via *Suzaku* software version 1.2. The reduction followed the prescriptions described in 'The Suzaku Data Reduction Guide' (also known as *the ABC guide*) provided by the *Suzaku* guest observer facility at the NASA/GSFC.[2] The screening was based on the following criteria: (1) only ASCA-grade 0, 2, 3, 4, 6 events are accumulated, while hot and flickering pixels were removed from the XIS image using the CLEANSIS script, (2) the time interval after the passage of South Atlantic Anomaly (T_SAA_HXD) is greater than 500 s, (3) the object is at least 5° and 20° above the rim of the Earth (ELV) during night and day, respectively. In addition, we also select the data with a cutoff rigidity (COR) larger than 6 GV. After this screening, the net exposure for good time intervals is 119.2 ks.

The XIS events were extracted from a circular region with a radius of $4.3'$ centered on the source peak, whereas the background was accumulated in an annulus with inner and outer radii of $4.9'$ and $6.3'$, respectively. We carefully checked that the use of different source and background regions did not affect the analysis results presented in the next sections, within $1\,\sigma$ uncertainties. The response (RMF) and auxiliary (ARF) files are produced using the analysis tools XISRMFGEN and XISSIMARFGEN developed by the *Suzaku* team, which are included in the software package HEAsoft version 6.12. We also checked whether our spectral fitting results (see §3) were consistent with what has been obtained using the 'standard' RMF and ARF files, provided for science working group members, for a point source placed on the nominal CCD position (AE_XI{0,1,2,3}_20060213.RMF and AE_XI{0,1,2,3}_XISNOM6_20060615.ARF). This was done after correcting for the degradation of the XIS response using the tool XISSCONTAMICALC.

2.1.2. HXD/PIN Data Reduction

The source spectrum and the light curves were extracted from the cleaned HXD/PIN event files (version 1.2). The HXD/PIN data are processed with basically the same screening criteria as those for the XIS, except that ELV $\geq 5°$ through night and day, T_SAA ≥ 500 s, and COR ≥ 8 GV. The HXD/PIN instrumental background spectra were generated from a time dependent model provided by the HXD instrument team for each observation (see Kokubun et al. 2007; Fukazawa et al. 2006 for more details; also see Kataoka et al. 2007 concerning the robustness of background subtraction of the HXD/PIN using the most recent response and background models). Both the source and background spectra were made with identical good time intervals (GTIs) and the exposure was corrected for detector deadtime of 6.3%. We used the response files version AE_HXD_PINXINOM_20060814.RSP, provided by the HXD instrumental team.

The time averaged HXD/PIN spectrum thus obtained is shown in Figure 1, plotted over the

[2]http://suzaku.gsfc.nasa.gov/docs/suzaku/analysis/abc. See also seven steps to the *Suzaku* data analysis at http://www.astro.isas.jaxa.jp/suzaku/analysis.

energy range 10–60 keV. HXD/PIN data below 12 keV have been ignored to avoid noise contamination near the lower threshold of the PIN diode. Also the data above 50 keV are discarded, as a detailed study of noise and background systematics is on-going above this energy. Figure 1 shows the total (PKS 1510−089 + observed background) spectrum, where the background includes both the instrumental (non X-ray) background and the contribution from the cosmic X-ray background (CXB) (Gruber et al. 1999; see also Frontera et al. 2007 for updated *BeppoSAX* results). Here the form of the CXB was taken as $9.0\times10^{-9}(\mathrm{E}/3\,\mathrm{keV})^{-0.29}\exp(-\mathrm{E}/40\,\mathrm{keV})\,\mathrm{erg\,cm^{-2}\,s^{-1}\,sr^{-1}\,keV^{-1}}$ and the observed spectrum was simulated assuming the PIN detector response to isotropic diffuse emission. When normalized to the field of view of the HXD/PIN instrument the effective flux of the CXB component is expected to be $9.0\times10^{-12}\,\mathrm{erg\,cm^{-2}\,s^{-1}}$ in the 12−50 keV band, which is about ∼20% of the PKS 1510−089 flux in the same energy bandpass.

Assuming that the spectral shape determined by the HXD/PIN (below 50 keV) would extend to 100 keV, the PKS 1510−089 flux would be $\sim 3.5\times10^{-11}\,\mathrm{erg\,cm^{2}\,s^{-1}}$ (50−100 keV) and could therefore ultimately be detected by the HXD/GSO detector. However, this is only a few percent of the GSO detector background and the study of this level of background systematics is still on-going by the HXD instrument team. Therefore, in this paper, we do not include the GSO data in the subsequent spectral fits. We also note that after 2006 May 24, bias voltages for 16 out of 64 PIN diodes (in the W0 unit) were reduced from 500 to 400 V to suppress the rapid increase of noise events caused by in-orbit radiation damage[3]. It is thus recommended that a careful comparison of the analysis results by including/excluding W0 unit be made. In this paper, we used all HXD/PIN sensors (including W0) because no differences were found between both analyses.

2.2. *Swift*

PKS 1510−089 was observed with *Swift* (Gehrels et al. 2004) 10 times in August 2006, as a Target of Opportunity (ToO) with a total duration of 24.3 ks. Table 1 summarizes the start and end times, and the exposure time of each observation. Note the *Swift* observations cover more than 18 days from August 4th to 22nd, and the first two observations are well within the range of the *Suzaku* observation. *Swift* carries three sets of instruments, the Burst Alert Telescope BAT (15−150 keV; Barthelmy et al. 2005), the X-ray Telescope XRT (0.3−10 keV; Burrows et al. 2005) and the Ultra-Violet/Optical Telescope UVOT (170−650 nm; Roming et al. 2005). Hereafter we only analyzed the XRT and the UVOT data because the source was not detected in the BAT exposures.

[3]http://www.astro.isas.jaxa.jp/suzaku/analysis/hxd/hxdresp

2.2.1. XRT Data Reduction

The *Swift* XRT data were all taken in Photon Counting mode (PC mode; Hill et al. 2004). The data were reduced by the XRT data analysis task XRTPIPELINE version 0.10.4, which is part of the HEASARC software package 6.1. Source photons were selected in a circle with a radius of $47''$ and background photons in a nearby source-free circle with a radius of $189''$. Photons were selected from the event file by XSELECT version 2.4. Spectra and light curves were corrected for losses due to dead columns (Abbey et al. 2006). Photons for the spectral analysis with grades 0−12 were selected and rebinned with GRPPHA version 3.0.0 having at least 20 photons per bin. The auxiliary response file was created by the XRT task XRTMKARF and the standard response file SWXPC0TO12_20010101V008.RMF. All spectra were analyzed in the 0.3−10.0 keV band using XSPEC version 12.3.0 (Arnaud 1996). Due to the low count rate, no correction for pileup was applied.

2.2.2. UVOT Data Reduction

Data from the UVOT and XRT were obtained simultaneously. The UVOT observing mode used one exposure in each of six optical and ultraviolet filters (in order; uvw2, v, uvm2, uvw1, u, and b) per *Swift* pointing (typically 5–15 minutes long). Event data were preserved for uvm2 and uvw2; for the other filters the data were converted to images on-board. Exposures were processed at the *Swift* Data Center. For this analysis, Level 1 event data and Level 2 sky-corrected image data were used. Photometry was performed using the HEASARC FTOOLs UVOTEVTLC for the event data (uvm2 and uvw2) and UVOTSOURCE for the image data (v, b, u and uvw1), and CALDB Version 2006-11-16. Since the source was relatively bright, the source aperture sizes were chosen to correspond to those used to determine the UVOT zero-points: $6''$ for the optical and $12''$ for the ultraviolet filters. Therefore, no aperture correction was required. A $25''$ background region was extracted from a blank area of the sky offset from the source. Several blank regions were tried; the choice of background region made only very minor differences to the final results. All event and image data were corrected for coincidence loss. All event data for a given orbit were binned together. A comparison of the event photometry to the ground-processed uvm2 and uvw2 images were made; the results were entirely consistent.

2.3. Ground-based observations

2.3.1. Optical

The photometric Optical/IR observations were carried out with two instruments: the Newtonian f/5, 0.4 m, Automatic Imaging Telescope (AIT) of the Perugia University Observatory, and the the Rapid Eye Mount (REM, see Zerbi et al. 2004) a robotic telescope located at the ESO Cerro

La Silla observatory in Chile[4]. The AIT is based on an equatorially mounted 0.4-m Newtonian reflector having a 0.15-m reflector solidly joined to it. The AIT is a robotic telescope equipped with a 192×165 pixels CCD array, thermoelectrically cooled with Peltier elements and with Johnson-Cousins BVRI filters utilized for photometry (Tosti et al. 1996).

The REM telescope has a Ritchey-Chretien configuration with a 60 cm f/2.2 primary and an overall f/8 focal ratio in a fast moving alt-azimuth mount providing two stable Nasmyth focal stations. At one of the two foci the telescope simultaneously feeds, by means of a dichroic, two cameras: REMIR for the NIR (see Conconi et al. 2004), and ROSS (see Tosti et al. 2004) for the optical. Both the cameras have a field of view of $10'' \times 10''$ and imaging capabilities with the usual NIR (z', J, H and K) and Johnson-Cousins VRI filters. All raw optical CCD frames obtained with the AIT and REM Telescopes, were corrected for dark, bias and flat field. Instrumental magnitudes were obtained via aperture photometry using DAOPHOT (Stetson 1988) and SEXTRACTOR (Bertin & Arnouts 1996). Calibration of the source magnitude was obtained by differential photometry with respect to the comparison star sequence reported by Villata et al. (1997) and Raiteri et al. (1998).

Also a few optical observations were carried out using a 70 cm telescope of the Landessternwarte in Heidelberg, Germany. Unfortunately most of the observations were not successful due to bad weather, and we only got data on August 1, just before the *Suzaku* observation started. We obtained B, R, I photometric measurements (2 points each, both consistent with each other within the relative photometric accuracies of 0.01 mag), suggesting no variations on a timescale of an hour within this night. The observation log and resultant magnitudes of PKS 1510−089 during 2006 August observations are summarized in Table 2.

2.3.2. Radio

The 1–22 GHz instantaneous radio spectrum of PKS 1510−089 was monitored with the 600-meter ring radio telescope RATAN-600 (Korolkov & Pariiskii 1979) of the Special Astrophysical Observatory, Russian Academy of Sciences, on 2006 August 9, 10, 11, 22, and 23. Observations were made at the Northern sector of the telescope with the secondary reflector of cabin No. 1. The continuum spectrum was measured at six different frequencies — 1, 2.3, 4.8, 7.7, 11, and 22 GHz — within two minutes in a transit mode. Details on the method of observation, data processing, and calibration are described in Kovalev et al. (1999). Since no significant time variations were found during these observations, the averaged data of the five independent spectral measurements are provided in Table 3.

PKS 1510−089 was also observed with the Australia Telescope Compact Array (ATCA). The ATCA consists of six 22 m diameter paraboloidal antennas (Frater, Brooks, & Whiteoak 1992) with

[4]http://www.rem.inaf.it

five antennas on a 3 km east-west track which has a 214 m north-south spur, and a sixth antenna fixed 3 km to the west of the east-west track. Snapshot observations were made with the ATCA on two dates. The first observations were made on 2006 July 11 at 1.4, 2.3, 4.8 and 8.6 GHz while the array was in 750B configuration, with a maximum baseline of 4.5 km. The second observations were made on August 4 in H168 configuration using the inner five telescopes, with a maximum baseline of 192 m, at frequencies of 18.5 and 19.5 GHz in addition to the same four frequencies as the first epoch. PKS 1934−638 was used as the primary flux density and bandpass calibrator at both epochs. Data were reduced with MIRIAD and the flux densities calculated under the assumption the source is point-like using the task UVFLUX (Sault et al. 1995). The flux densities at both the first and the second epochs are summarized in Table 3. The errors in the flux densities include the intrinsic scatter in the data and a conservative allowance of 5% for systematic variation in the flux density scale (Tingay et al. 2003).

3. Results

3.1. *Suzaku*

During the *Suzaku* observation (August 2−5; Table 1), PKS 1510−089 was in a relatively bright state with the average net count rates of 4 XISs, measured in the 0.4−10 keV range, of $2.388 \pm 0.003\,\mathrm{cts\,s^{-1}}$. For the PIN detector, the net average source count rate in the 12−40 keV band was $0.105 \pm 0.003\,\mathrm{cts\,s^{-1}}$, compared to the PIN background (non X-ray background) rate of $0.425\,\mathrm{cts\,s^{-1}}$. Figure 2 shows count rate variations during the *Suzaku* observation. The light curves of the 4 XISs and the HXD/PIN detectors are shown separately in different energy bands; 0.4−1 keV (*upper*; XIS), 3−10 keV (*middle*; XIS) and 12−40 keV (*lower*; HXD/PIN). This clearly indicates different variability properties: count rates decreased above 3 keV (*middle* and *bottom* panel), while it reached a delayed maximum ∼1.5 day from the start of the *Suzaku* observation for the 0.4−1 keV band.

Spectral evolution during the observation is best illustrated as a correlation between the source brightness and the hardness ratio. Figure 3 shows the count rate (sum of 0.4−1.0 keV and 3−10 keV counts) versus hardness ratio, defined as the ratio of the XIS count rates at 3−10 keV to those at the 0.4−1.0 keV. This suggests a spectral evolution with the spectrum hardening as the source becomes brighter, although the correlation is rather loose, especially when the source is in the lower state of the activity (e.g., when the sum of 0.4−1 keV and 3−10 keV count rates is less than $1.2\,\mathrm{ct\,s^{-1}}$). In addition, the hardness parameter is not a linear function of the source brightness, at least for the relatively short timescale of the *Suzaku* observation (i.e., within three days). Again, this may suggest that more than just one spectral component contributes to the observed X-ray emission of PKS 1510−089.

The XIS and HXD/PIN background subtracted spectra were fitted using XSPEC v11.3.2, including data within the energy range 0.3−50 keV. We binned the XIS spectra to a minimum of

400 counts per bin to enable the use of the χ^2 minimization statistic. The Galactic absorption toward PKS 1510−089 is taken to be $N_{\rm H} = 7.88{\times}10^{20}\,{\rm cm}^{-2}$ (Lockman & Savage 1995). All errors are quoted at the 68.3% (1σ) confidence level for the parameter of interest unless otherwise stated. All the fits in this section are restricted to the energy range 0.5−12 keV (XIS 0, 2, 3: FI chips), 0.3−9 keV (XIS 1: BI chip) and 12−50 keV (HXD/PIN). In the following analysis, we fixed the relative normalization of the XISs/PIN at 1.13, which is carefully determined from calibration using the Crab nebula, pointed at the XIS nominal position (*Suzaku* internal report; JX-ISAS-SUZAKU-MEMO-2006-40 by M. Ishida).

Figure 4 shows 4 XISs + HXD/PIN spectra with residuals to the best-fit power-law model determined using data between 2 and 50 keV. The residuals of Figure 4 indicate that the spectrum exhibits significant soft excess emission below 2 keV. If we model the overall X-ray spectrum between 0.3 and 50 keV with a simple power-law function modified by the Galactic absorption, we obtain the best-fit photon index $\Gamma_{\rm high} = 1.30$, but the fit is statistically unacceptable with a χ^2/d.o.f. of 705/585 (Table 4). To represent the concave shape of the observed X-ray spectrum, we first consider a double power-law function (PL+PL) in which the soft X-ray excess is due to a steep power-law component with the photon index $\Gamma_{\rm low} \simeq 2.7$. This provides an acceptable fit with χ^2/d.o.f. = 536/585, although the wavy structure still remains, especially below 1 keV.

Hence we considered an alternative fit consisting of a hard power-law function (PL) with $\Gamma_{\rm hard} = 1.23$ and a blackbody (BB) component or a disk blackbody (DB; Mitsuda et al. 1984) feature. Both models give similarly good representation of the data, with the best χ^2/d.o.f. = 515/585 for the latter (Table 4). The improvement of the χ^2 statistic is significant at more than the 99.9 % confidence level when compared to the PL+PL model described above ($\Delta\,\chi^2 \simeq 20$ for 583 d.o.f). The temperature of the introduced thermal component is fitted as $kT \simeq 0.2$ keV. Figure 5 shows an absorption corrected νF_ν spectrum deconvolved with this PL+DB model. The integrated luminosity of this blackbody-type emission is $L_{\rm BB} \simeq (2.6 \pm 0.2){\times}10^{44}\,{\rm erg\,s}^{-1}$.

3.2. *Swift*

The deep *Suzaku* observations of PKS 1510−089 over three days (120 ks in total) are well complemented by the *Swift*/XRT observation for monitoring the long-term variability of this source on the week-long scale. In addition, the first two observations made by *Swift* were simultaneous with *Suzaku* (see Table 1), and thus provide an important opportunity for the cross-calibration of results between the two instruments. Since the effective area of *Swift*/XRT is less than 10% of the XIS onboard *Suzaku* in the 0.5−10 keV range, detailed spectral modeling is difficult using the *Swift* data alone. Furthermore, the average exposure for the *Swift* segment was only a few kilosecond, which was much less than the *Suzaku* exposure of 120 ks. We therefore fit the XRT data simply with a power-law function in the energy band 0.3−10 keV, modified by the Galactic absorption.

Figure 6 compares the variations of the X-ray flux and changes in the power-law spectral

photon index as a function of time. Here the observation time is measured from the start of the *Suzaku* observation, i.e., 2006 August 2, 09:31 UT. Note the wide range of source variability (about a factor of two) on a week-scale, which was not observed with *Suzaku*. The blue lines in this figure show the time coverage and the best fit parameter determined by *Suzaku* (the two dashed lines show the $1\,\sigma$ uncertainty of the *Suzaku* parameters). We confirm that the results obtained with *Suzaku* and *Swift* are perfectly consistent with each other. Figure 7 shows the relation between the $0.5-10$ keV flux versus photon index measured by *Swift*/XRT (the data from August 10 were excluded as they have large statistical uncertainties due to the short exposure; see Table 1). Clearly the X-ray spectrum becomes harder when the source gets brighter. Such a trend is often observed in high-frequency peaked BL Lacs (e.g., Kataoka et al. 1999), but has not previously been observed so clearly in a quasar hosted blazar such as PKS 1510−089.

Thanks to the excellent sensitivity and wideband coverage of *Swift*/UVOT, even relatively short 1 ks exposures provide the deepest UV-optical measurement ever reported for this source in the literature. To cover as much bandpass as possible, we used all the filters (v, b, u, uvw1, uvm2, uvw2) for all 10 observations (Table 1). The fluxes in each filter were corrected for galactic extinction following the procedure described in Cardelli, Clayton, & Mathis (1989): Galactic extinction with $R_V = 3.1$ and $E_{B-V} = 0.097$ taken from Schlegel et al. (1998). We note that the expected extinction value is somewhat higher than the one given by Burstein and Heiles (1982; E_{B-V} between 0.06 and 0.09). We generated a list of the amount of extinction that needs to be accounted for in each filter, $A_\lambda = E_{B-V} \times [a\ R_{\rm V}\ +\ b]$ where a and b are constants summarized in Table 5. Resultant correction factors to each filters were $\times$1.32, 1.45, 1.56, 1.82, 1.91 and 2.09, respectively for v, b, u, uvw1, uvm2, uvw2 band filters. The extinction-corrected light curves thus produced are shown in Figure 8. In contrast to the X-ray light curve (Figure 6), no significant variability was detected throughout the 2006 August campaign.

Finally, Figure 9 shows the combined optical/UV spectrum of PKS 1510−089 taken during the campaign. *Red circles* show the average *Swift*/UVOT data, whereas *green* and *blue* points show data taken by REM and Landessternwarte, Heidelberg. Note the excellent agreement between *Swift*/UVOT and other telescopes at optical wavelengths. The overall trend of the optical/UV continuum is that the flux density (F_ν in mJy) decreases with increasing frequency, such that $F_\nu \propto \nu^{-0.57}$. Also, it appears that the spectrum shows an interesting dip/discontinuity around $\nu \sim 10^{14.7}$ Hz and $10^{15.0}$ Hz. No discontinuity is evident in the combined infrared/optical/UV SED and line flux measurements (e.g., Mg II) provided by Malkan & Moore (1986). However, strong line-emission present in a single Swift/UVOT filter can produce an apparent discontinuity. The discrepancy may also be explained by the fact that the observations reported by Malkan & Moore (1986) were obtained over several epochs.

4. Discussion

4.1. Flat X-ray Continuum and Spectral Evolution

In the previous sections we have presented temporal and spectral analyses of *Suzaku* and *Swift* observations of PKS 1510−089 in August 2006. The great advantage of using *all* the *Suzaku* and *Swift* instruments is that we can resolve the spectral evolution on different time scales, from hours (*Suzaku*) to weeks (*Swift*). In particular, our campaign provided the first detection of time variability as short as the day-scale in the hard X-ray energy band (12−40 keV). During the *Suzaku* observations, PKS 1510−089 was in a relatively high state with an average flux of $F_{2-10\mathrm{keV}} \sim 1.1\times10^{-11}\,\mathrm{erg\,cm^{-2}\,s^{-1}}$, that gradually decreased by about 10% over the duration of the observation. Historically, the flux observed with *Suzaku* is more than two times higher than that observed with *BeppoSAX* in 1998 ($5.2\times10^{-12}\,\mathrm{erg\,cm^{-2}\,s^{-1}}$) or with *ASCA* in 1996 ($8.6\times10^{-12}\,\mathrm{erg\,cm^{-2}\,s^{-1}}$). *Swift*/XRT sampled a range of continuum fluxes during the 18 days of the campaign, detecting significant spectral evolution with the photon index Γ changing from 1.2 to 1.5.

The observed photon index is significantly lower than that of radio-loud quasars ($<\Gamma> = 1.66 \pm 0.07$; Lawson et al. 1992; Cappi et al. 1997) or radio-quiet quasars ($<\Gamma> = 1.90 \pm 0.11$; Lawson et al. 1992; Williams et al. 1992), and is more similar to the ones observed in high-redshift quasars. For example, in the sample of 16 radio-loud quasars at $z > 2$ considered by Page et al. (2005), four sources have hard spectra with $\Gamma = 1.4$. (see also Tavecchio et al. 2000 for 0836+710 and Sambruna et al. 2006 for the *Swift* blazar J0746+2449 with $\Gamma \simeq 1.3$). Such hard X-ray spectra pose a challenge to the 'standard' shock models of particle acceleration, because they imply a very flat electron energy distribution. As long as the X-ray emission is due to the low-energy tail of the ERC spectral component, the photon index $\Gamma = 1.2$ corresponds to the electron energy distribution $N(\gamma) \propto \gamma^{-1.4}$, where γ is the Lorentz factor of the ultrarelativistic (radiating) electrons.

This may suggest that shocks — if indeed they are responsible for accelerating the jet particles — can produce relativistic electrons with an energy spectrum much harder than the 'canonical' power-law distribution $N(\gamma) \propto \gamma^{-2}$, or that another mechanism energizes the electrons, at least at the low energies, $\gamma \leq 10$, typically involved in production of the X-ray emission within the ERC model (e.g., Tavecchio et al. 2007). The latter possibility was discussed by Sikora et al. (2002) who assumed a double power-law form of the injected ('freshly accelerated') electrons, with the break energy $\gamma_{\mathrm{br}} \sim 10^3$ corresponding to the anticipated threshold of diffusive shock acceleration[5]. Below that energy, the electrons must be accelerated by a different mechanism, e.g., involving instabilities driven by shock-reflected ions (Hoshino et al. 1992) or magnetic reconnection (Romanova & Lovelace 1992). These 'alternative' processes can possibly account for the electron distribution being harder than $\propto \gamma^{-2}$. The X-ray emission of PKS 1510−089 discussed here provides direct constraints on this crucial low-energy population of ultrarelativistic electrons in quasar jets. At the other end of the

[5]See in this context Stawarz et al. (2007) for the case of particle acceleration at mildly-relativistic shocks in large-scale jets.

spectrum of the Compton component, archival EGRET (and, in the future, *GLAST*) observations may be used to constrain the high-energy tail of the accelerated electrons.

In this context, it is interesting to revisit the spectral evolution detected with the *Swift* XRT in PKS 1510−089. In general, the trend established for FSRQs is that only little X-ray variability is observed on short time-scales of hours to days. Even on longer time-scales the X-ray variations in FSRQs are usually small, and the X-ray spectral shape is almost constant. The best example for such a behavior is 3C 279, where the X-ray slope changed only a little during the historical outburst in 1988, from $\Gamma = 1.70 \pm 0.06$ to 1.58 ± 0.03 (Makino et al. 1989). However, exceptions were found recently in several distant quasars. For example, RBS 315 changed the X-ray spectral slope from $\Gamma = 1.3$ to 1.5 between two observations separated by three years (Tavecchio et al. 2007). Also, the hard X-ray spectrum of 0836+710 softened from $\Gamma \simeq 1.4$ (as measured by *BeppoSAX*; Tavecchio et al. 2000) to $\Gamma \simeq 1.8$ (*Swift* observations; Sambruna et al. 2007).

Such a variability pattern may simply imply that the distribution of ultrarelativistic electrons at low energies changes (though not dramatically) in some sources. Another explanation, however, is that this spectral shape remains roughly constant, but that the amount of contamination from the soft excess emission varies, affecting the spectral fitting parameters at higher energies ($E \geq 2\,\mathrm{keV}$). In fact, we showed that the photon index became a little steeper ($\Delta\Gamma \simeq 0.1$; Table 4) when we fit the spectrum with a simple power-law function. This suggests that spectral evolution of PKS 1510−089 may be explained by the soft excess emission being more important when the source gets fainter, and becoming almost completely 'hidden' behind the hard X-ray power-law ($\Gamma_{\mathrm{hard}} \simeq 1.2$) when the source gets brighter.

4.2. Modeling the overall SED

Figure 10 shows the overall spectral energy distribution (SED) of PKS 1510−089 during the 2006 August campaign. Filled red circles represent simultaneous data from the radio (RATAN-600 and ATCA), optical (*Swift* UVOT, REM and Heidelberg), and the X-ray (*Suzaku*) observations. Historical data taken from the radio (NED and CATS), FIR (*IRAS*, Tanner et al. 1996), optical (NED), soft X-ray (*ROSAT*; Singh, Shrader & George 1997) and γ-ray (EGRET; Hartman et al. 1999) observations are also plotted as black points or blue bow-ties. Figure 10 implies that the synchrotron component of PKS 1510−089 peaks most likely around 10^{12-14} Hz, while the excess at NIR frequencies may be due to the starlight of the host, and the excess at FIR due to dust radiation from the nuclear torus. Meanwhile, our UVOT/REM/Heidelberg data show the 'rising' emission in the frequency range between $10^{14.4}$ and $10^{15.2}$Hz, with $\nu F_\nu \propto \nu^{0.43}$ (§3.2.2). As already suggested in the literature (e.g., Malkan & Moore 1986; Pian & Treves 1993), this is most likely a manifestation of a strong 'UV excess' ('blue-bump'), which is thought to be produced by the accretion disk and/or corona near the central black hole of PKS 1510−089. Apparently, these optical/UV data do not join smoothly with the X-ray–to–γ-ray spectrum, which is due to the non-thermal ERC jet radiation. Also note that the X-ray spectrum softens at low energies due to the

presence of soft excess emission, as suggested by the detailed spectral fitting in Figures 4 and 5.

To reproduce the overall SED of PKS 1510−089, we applied the numerical model *BLAZAR* developed in Moderski, Sikora & Błażejowski (2003), updated for the correct treatment of the Klein-Nishina regime (Moderski et al. 2005). The code is based on a model in which the non-thermal flares in blazars are produced in thin shells propagating down a conical jet with relativistic velocities. The production of non-thermal radiation is assumed to be dominated by electrons and positrons which are accelerated directly, rather than injected by pair cascades. The code traces the time evolution of the synchrotron and IC components, where both the synchrotron and external photons are considered as seed radiation fields contributing to the IC process. We assumed that the electrons are injected by the shock formed at a distance $0.5r_{\rm sh}$, propagating with a Lorentz factor $\Gamma_{\rm sh}$, and decaying at $r = r_{\rm sh}$, and that the injection function takes the broken power-law form

$$Q_\gamma = K_e \frac{1}{\gamma^p + \gamma_{\rm br}^{p-q}\ \gamma^q}\,, \tag{1}$$

where K_e is the normalization factor, p and q are spectral indices of the injection function at the low and high energy limits, respectively, and $\gamma_{\rm br}$ is the break energy.

Co-moving energy density of the external radiation is approximated via

$$u'_{\rm ext} = \frac{4}{3}\,\Gamma_{\rm sh}^2\ \frac{L_{\rm ext}}{4\pi c r_{\rm ext}^2}\ \frac{1}{1+(r/r_{\rm ext})^n}\,, \tag{2}$$

where $L_{\rm ext}$ and $r_{\rm ext}$ are the total luminosity and the scale (spatial extent) of the considered external photon field, respectively, and $n \geq 2$. We investigated radiation fields from both the dusty torus and the BLR and found that Comptonization of the former better reproduces the observed spectrum. Our fit of PKS 1510-089 is shown on Figure 10 and the model parameters are specified in the figure caption and in Table 6 ('Model A'). The presented model is a snapshot at the maximum of the flare which corresponds roughly to the distance $r_{\rm sh}$. Note that $r_{\rm sh} > r_{\rm BLR}$, but $r_{\rm sh}$ is still much below the radio photospheres and the observed flat-spectrum radio emission originates from the superposition of more distant, self-absorbed portions of the outflow.

4.3. Energetics and Pair Content

In order to derive the power and pair content of a jet, dynamics and structure of the shock must be specified. We adopt here internal shock scenario and assume that shells with relativistic plasma represent regions enclosed between the reverse and forward shock fronts. Such a structure is formed by colliding inhomogeneities propagating down the jet with different Lorentz factors. In this model, the light curves are produced by a sequence of shocks with a range of locations and lifetimes (Spada et al. 2000). Our fit presented in Figure 10 shows the radiative output of the shock operating over a distance range $\Delta r = 0.5 \times 10^{18}$cm, starting at 0.5×10^{18}cm and decaying at $r_{\rm sh} = 10^{18}$cm. The amount of electrons/positrons injected into shell by the end of the shock

operation is

$$N_{e,\rm inj} = t'_{\rm sh}\int_{\gamma_{\rm min}} Q_\gamma d\gamma \simeq \frac{\Delta r}{c\Gamma_{\rm sh}}\frac{K_e}{(p-1)\gamma_{\rm min}^{p-1}} \simeq 2.9\times 10^{53}\,, \tag{3}$$

where $t'_{\rm sh} = \Delta r/(c\Gamma_{\rm sh})$ is the lifetime of the shock as measured in the shock (discontinuity surface) rest frame.

The electrons/positrons are accelerated/injected resulting in an average energy $\bar\gamma_{\rm inj} = \int Q_\gamma\gamma d\gamma/\int Q_\gamma d\gamma \simeq 22$ that follows from the model parameters as given in the caption of Figure 10 and in Table 6. Assuming that this energy is taken from protons, we have the electron+positron to proton ratio

$$\frac{N_e}{N_p} = \eta_e\frac{m_p(\bar\gamma_p-1)}{m_e\bar\gamma_{\rm inj}}\,, \tag{4}$$

where η_e is the fraction of the proton thermal energy tapped by electrons and positrons. The value of $\bar\gamma_p - 1$, which actually represents efficiency of the energy dissipation, depends on properties and speeds of colliding inhomogeneities, and is largest if they have same rest densities and masses. In this case, assuming $\Gamma_2 > \Gamma_1 \gg 1$,

$$\bar\gamma_p - 1 = \frac{(\sqrt{\Gamma_2/\Gamma_1}-1)^2}{2\sqrt{\Gamma_2/\Gamma_1}}\,, \tag{5}$$

and $\Gamma_{\rm sh} = \sqrt{\Gamma_1\Gamma_2}$ (Moderski et al. 2004).

We assume hereafter $\Gamma_1 = 10$ and $\Gamma_2 = 40$ and using Eqs. (4) and (5) obtain $N_e/N_p \sim 20\eta_e$. In this case the rest frame width of the shell by the end of the shock evolution is $\lambda' \simeq 0.4(\Delta r/\Gamma_{\rm sh}) \simeq 1.1\times 10^{16}$cm (see Appendix in Moderski et al. 2004), and density of electrons/positrons is $n'_e = N_{e,\rm inj}/(\pi R^2\lambda')$, where $R = \theta_{\rm jet} r$ is the cross-sectional radius of a jet. Using these relations one can estimate energy flux carried by protons,

$$L_p \simeq n'_p m_p c^3\pi R^2\Gamma_{\rm sh}^2 \sim n'_e\frac{N_p}{N_e}m_p c^3\pi R^2\Gamma_{\rm sh}^2 \sim 2.2\times 10^{46}\,(1-\eta_e)/\eta_e\,{\rm erg\,s^{-1}}\,. \tag{6}$$

This can be compared with the energy flux carried by magnetic fields

$$L_B \simeq \frac{B^2}{8\pi}c\pi R^2\Gamma_{\rm sh}^2 \simeq 6.3\times 10^{45}\,{\rm erg\,s^{-1}}\,, \tag{7}$$

and by electrons and positrons

$$L_e \simeq n'_e\bar\gamma_{\rm inj} m_e c^3\pi R^2\Gamma_{\rm sh}^2 \simeq 5.6\times 10^{45}\,{\rm erg\,s^{-1}}\,, \tag{8}$$

where L_e is estimated without taking into account radiative losses of relativistic electrons/positrons and therefore is overestimated by a factor ~ 4.

4.4. Soft X-ray Excess

Figure 11 shows in detail the optical–to–X-ray region of the SED. The hump on the left mimic an excess emission from the dusty torus as suggested by *IRAS* (Tanner et al. 1996) with a dust temperature of $kT \simeq 0.2\,\mathrm{eV}$ and $L_{\rm dust} \simeq 3.7{\times}10^{45}\,\mathrm{erg\,s^{-1}}$ (see also Table 6). The hump on the middle is our attempt to account for the blue bump assuming an inner-disk temperature of $kT \simeq 13\,\mathrm{eV}$ and $L_{\rm disk} \simeq 4{\times}10^{45}\,\mathrm{erg\,s^{-1}}$. We note here that the bolometric accretion luminosity is larger than this at least by a factor two, since more realistic models of accretion disks produce modified black body radiation, with extended high energy tails and additional contribution from more distant, cooler portions of a disk.

From the spectral fitting of the *Suzaku* data, we showed in §3.1 and Table 4 that the soft X-ray excess may be represented either by a steep power-law ($\Gamma_{\rm low} \simeq 2.7$) or a black-body–type emission of $kT \simeq 0.2\,\mathrm{keV}$. We investigate below whether such excess can be produced by a bulk Comptonization of external diffuse radiation by cold inhomogeneities / density enhancements prior to their collisions. At $r > r_{\rm BLR}$ density of the diffuse external UV radiation is very small, while bulk-Compton features from upscatterings of dust infrared radiation falls into the invisible extreme-UV band. However, if acceleration of a jet has already occurred at $r \leq r_{\rm BLR}$, upscattering of photons from broad-emission line region should lead to formation of bulk Compton features, with peaks located around $\nu_{\rm BC,i} \sim \mathcal{D}_{\rm i}\Gamma_{\rm i}\nu_{\rm UV}/(1+z)$ and luminosities

$$L_{\rm BC,i} = \frac{4}{3} c\sigma_{\rm T} u_{\rm BLR} \Gamma_{\rm i}^2 \mathcal{D}_{\rm i}^4 N_{e,\rm obs,i}\,, \tag{9}$$

where $i = 1, 2$, $u_{\rm BLR}$ is the energy density of the broad emission lines, $\mathcal{D}_{\rm i}$ is the Doppler factor, and $N_{e,\rm obs,i}$ is the number of electrons and positrons contributing to the bulk-Compton radiation at a given instant (see Moderski et al. 2004). Above formulas apply to cylindrical jets and must be modified if used as approximations for conical jets. For the conical jets the Doppler factor should be replaced by the 'effective' Doppler factor which for $\theta_{\rm obs} \leq \theta_{\rm jet}$ is $\mathcal{D}_{\rm i} = \kappa\Gamma_{\rm i}$, where $1 < \kappa < 2$. For our model parameters

$$N_{e,\rm obs,1} \simeq \frac{N_{\rm inj}}{2}\,\frac{r_{\rm BLR}}{\lambda_0 \mathcal{D}_1}\,, \tag{10}$$

and

$$N_{e,\rm obs,2} \simeq \frac{N_{\rm inj}}{2}\,\frac{r_{\rm BLR}}{\lambda_0 \mathcal{D}_2}\,\frac{\Gamma_{\rm sh}^2}{2\Gamma_2^2}\,, \tag{11}$$

where λ_0 is the proper width (longitudinal size) of the cold inhomogeneities (see Appendix A3 in Moderski et al. 2004); the factor $r_{\rm BLR}/(\lambda_0\mathcal{D}_{\rm i})$ is the fraction of particles observed at a given instant and takes into account that the source is observed as being stretched to the size $\lambda_0\mathcal{D}_{\rm i}$ which is larger than $r_{\rm BLR}$; and the extra factor in the last equation, $\Gamma_{\rm sh}^2/(2\Gamma_2^2)$, is the fraction of particles enclosed within the Doppler beam. With the above approximations and $\kappa = 1.5$ our model predicts location of the bulk-Compton features at ~ 1 keV and ~ 18 keV, and luminosities of $\sim 2\times10^{44}\,\mathrm{erg\,s^{-1}}$ and $2\times10^{46}\,\mathrm{erg\,s^{-1}}$, respectively. Comparing these luminosities with luminosities of nonthermal radiation we conclude that within the uncerainties regarding the details of the jet

geometry and model parameters, bulk-Compton radiation produced by slower inhomogeneities is sufficiently luminous to be responsible for the soft X-ray excess observed by *Suzaku*, while the faster one can be tentatively identified with a small excess at ~ 18 keV seen in Fig. 11.

4.5. On Alternative Models

Very hard X-ray spectrum measured by *Suzaku* — with $\Gamma_{\rm X-ray} < 1.5$ — excludes models in which X-rays are produced by synchrotron radiation of the secondary ultrarelativistic population of electrons/positrons predicted by hadronic models, whereas the large luminosity ratio of the high to low energy components challenges the SSC models via enforcing magnetic fields much below the equipartition value (Moderski & Sikora 2007). No such constraints apply to ERC models, provided jets are sufficiently relativistic. Furthermore, in the comoving frame of a jet moving with a Lorentz factor ≥ 6, the energy density of seed photon fields is dominated by broad emission lines or infrared radiation of dust (depending on a distance of the source from the black hole), rather than by locally produced synchrotron radiation (Sikora et al. 1994). On the other hand, leptonic content of jets in the SSC models can be much smaller than in the ERC models, and therefore such models can easily avoid production of bulk-Compton features which in the context of ERC models are predicted to be prominent (Moderski et al. 2004) but so far were not observationally confirmed. However, that concern applies only to ERC models with the seed photons from the BLR. Production of similar high energy spectra but at larger distances where external diffuse radiation field is dominated by near/mid infrared radiation involves smaller leptonic content and therefore weaker bulk-Compton features (Sikora et al., in preparation). Furthermore, the predicted bulk-Compton features can be weaker in a scenario where the jet may still be in the acceleration phase while traversing the BLR (see Komissarov et al. 2007 and refs. therein).

If the latter is the case, the soft X-ray excess in PKS 1510−089 cannot originate from the bulk-Compton process. A possible alternative origin of the observed soft X-ray excess may be then provided by central regions of the accertion flow (Done & Nayakshin 2007), as seems to be the case in many non-blazar AGNs (Crummy et al. 2007 and refs. therein; see also Figure 6 in Laor et al. 1997).

Yet another possibility for the origin of the observed soft X-ray excess would be due to a more significant contribution of the SSC component in a frequency range between the synchrotron and ERC peaks, that would remain essentially invisible in the UV and hard X-ray bandpasses. In fact, we find that the collected data for PKS 1510−089 are consistent with another set of model parameters than discussed previously (§ 4.2-4.3), for which the soft X-ray excess is due to a combination of (I) the tail of the synchrotron component, (II) the ERC, and (III) the SSC emission falling in the soft X-ray band (Figures 12 and 13; see also parameters of 'Model B' in Table 6). Some discrepancies seen at $10^{17}-10^{18}$ Hz are probably due to the mismatch of spectral slopes between the expected index of the SSC component ($\Gamma \simeq 2$) and the observed, steep excess emission (kT

$\simeq 0.2\,\mathrm{keV}$ or $\Gamma_{\mathrm{low}} \simeq 2.7$). A steeper power-law contribution might naturally be provided just by the high-energy tail of the synchrotron emission, as often observed in low-frequency peaked blazars (e.g., Madejski et al. 1999; Tanihata et al. 2000; Tagliaferri et al. 2000). However, we note that extrapolation of this power-law to lower frequencies overpredicts the observed IR/optical continuum about an order of magnitude. Still, even if any of the above models proves to be more appropriate as a description of the soft excess, the results obtained in Sec. 4.4 for the bulk-Compton features should be considered as upper limits which would then imply that the Lorentz factor of the jet is lower in the BLR region than at distances where the nonthermal radiation is produced.

5. Conclusions

We have presented a detailed analysis of the data for the powerful γ-ray – emitting quasar PKS 1510−089 obtained with *Suzaku*, *Swift* XRT/UVOT, and ground-based optical (REM, Heidelberg) and radio (RATAN-600, ATCA) telescopes. Observations were conducted in 2006 August as an intensive multiwavelength three-week–long campaign. An excellent broadband spectrum of the source was uniquely constructed, covering ten decades in frequency, from $10^9\,\mathrm{Hz}$ to $10^{19}\,\mathrm{Hz}$. Our major findings are as follows:

(i). Deep *Suzaku* observations indicate moderate X-ray variability of PKS 1510−089 on the timescale of days, although differing in nature between the low (0.4−1 keV) and high ($\geq 3\,\mathrm{keV}$) energy bands.

(ii). The X-ray spectrum of PKS 1510−089 is well represented by an extremely hard power-law (photon index $\Gamma \simeq 1.2$) augmented by a blackbody-type component (temperature $kT \simeq 0.2\,\mathrm{keV}$) that accounts for the excess emission below 1 keV.

(iii). *Swift*/XRT observations reveal significant spectral evolution of the X-ray emission on the timescale of a week: the X-ray spectrum becomes harder as the source gets brighter.

(iv). Using ERC model we found that best fit of the broad-band spectrum is obtained by assuming that nonthermal radiation is produced at $r > r_{\mathrm{BLR}}$ where external diffuse radiation field is dominated by IR radiation of hot dust.

(v). The model predicts that the electron to proton ratio $N_e/N_p \sim 10$ and that the power of the jet is dominated by protons.

(vi). Prior to collisions and formation of shocks, density inhomogeneities interact with the BLR light and produce bulk-Compton features which tentatively can be identified with the features observed in the *Suzaku* spectra: soft X-ray excess seen below ~ 1 keV, and another, marginally significant spectral feature at ~ 18 keV.

(vii). Alternatively, the soft X-ray excess can be explained as a contribution of SSC component or it can just be identified with the soft X-ray excess often observed in the non-blazar AGN.

We are grateful to all the *Suzaku* members who helped us in analyzing the data. We also thank all the *Swift* members (especially Neil Gehrels who approved the target) for performing the ToO observations. We thank an anonymous referee for his/her helpful comments which helped clarify many of the issues presented in this paper. This work is sponsored at PSU by NASA contract NAS 5-00136. G.T. and D.I. thank the REM team for the support received during the observations. RATAN–600 observations were partly supported by the Russian Foundation for Basic Research (projects 05–02–17377). The ATCA is part of the Australia Telescope which is funded by the Commonwealth of Australia for operation as a National Facility managed by CSIRO. P.G.E. thanks Mark Wieringa for assistance with the ATCA observations. The authors made use of the database CATS (Verkhodanov et al. 1997) of the Special Astrophysical Observatory. This research has made use of the NASA/IPAC Extragalactic Database (NED) which is operated by the Jet Propulsion Laboratory, California Institute of Technology, under contract with the National Aeronautics and Space Administration. J.K. and N.K. acknowledge support by JSPS KAKENHI (19204017/14GS0211). G.M. and Ł.S. acknowledge the support by the Department of Energy contract to SLAC no. DE-AC3-76SF00515. M.S. and R.M. were partially supported by MEiN grant 1-P03D-00928. G.M. acknowledges the support via the NASA Suzaku grant no. NNX07AB05G. Y.Y.K is a Research Fellow of the Alexander von Humboldt Foundation. Ł.S. was supported by MEiN through the research project 1-P03D-003-29 from 2005 to 2008.

REFERENCES

Abbey, T. 2006, proceedings of the conference "The X-ray Universe", El Escorial, 2005, ESA-SP 604, 943

Arnaud, K. A. 1996, ASP Conf. Ser. 101: Astronomical Data Analysis Software and Systems V, 101, 17

Baars, J, W. M, Genzel, R., Pauliny-Toth, I. I. K, Witzel, A. 1977, A&A, 61, 99

Barthelmy, S. D., et al. 2005, Space Sci. Rev., 120, 143

Begelman, M. C., & Sikora, M. 1987, ApJ, 322, 650

Bertin E., & Arnouts S. 1996, A&AS, 117, 393

Burrows, D. N., et al. 2005, Space Sci. Rev., 120, 165

Burstein, D., & Heiles, C. 1982, AJ, 87, 1165

Cappi, M., et al. 1997, ApJ, 478, 492

Cardelli, J. A., Clayton, G. C., & Mathis, J. S. 1989, ApJ, 345, 245

Celotti, A., Padovani, P., & Ghisellini, G. 1997, MNRAS, 286, 415

Celotti, A., Ghisellini, G., & Fabian, A. C. 2007, MNRAS, 375, 417

Conconi, P., et al. 2004, Proc. SPIE, 5492, 1602

Crummy, J., Fabian, A. C., Gallo, L., & Ross, R. R. 2006, MNRAS, 365, 1067

Dermer, C. D., & Schlickeiser, R. 1993, ApJ, 416, 458

Done, C., & Nayakshin, S. 2007, MNRAS, 377, L59

Eisloffel, J., & Mundt, R., 1997, AJ, 114, 280

Georganopoulos, M., Kazanas, D., Perlman, E., & Stecker, F. 2005, ApJ, 625, 656

Fukazawa, Y., et al. 2006, Proc. SPIE, 6266, 75

Frater, R. H., Brooks, J. W., & Whiteoak, J. B. 1992, J. Electrical and Electronics Eng. Australia, 12, 103

Frontera, F., et al. 2007, ApJ, in press (astro-ph/0611228)

Gambill, J. K., et al. 2003, A&A, 401, 505

Gehrels, N., et al. 2004, ApJ, 611, 1005

Ghisellini, G., Celotti, A., Fossati, G., Maraschi, L., & Comastri, A. 1998, MNRAS, 301, 451

Gruber, D. E., Matteson, J. L., Peterson, L. E., & Jung, G. V. 1999, ApJ, 520, 124

Hartman R.C., et al. 1999, ApJS, 123, 79

Hill, J.E., et al., 2004, Proc. SPIE, 5165, 217

Hirotani, K. 2005, ApJ, 619, 73

Homan D. C., et al. 2001, ApJ, 549, 840

Hoshino, A., Arons, J., Gallant, Y. A., & Langdon, A. B. 1992, ApJ, 390, 454

Jorstad, S. G., et al. 2005, AJ, 130, 1418

Kataoka, J., et al. 1999, ApJ, 514, 138

Kataoka, J., et al. 2001, ApJ, 560, 659

Kataoka, J., et al. 2007, PASJ, 59, 279

Koide, S., Meier, D., Shibata, K., & Kudoh, T. 1999, ApJ, 536, 668

Kokubun, M., et al. 2007, PASJ, 59, 53

Korolkov, D. V., & Pariiskii, I. N. 1979, S&T, 57, 324

Kovalev, Y. Y., Nizhelsky, N. A., Kovalev, Yu. A., Berlin, A. B., Zhekanis, G. V., Mingaliev, M. G., & Bogdantsov, A. V. 1999, A&AS, 139, 545

Komissarov, S.S., Barkov, M.V., Vlahakis, N., & Königl, A. 2007, MNRAS, in press [arXiv:astro-ph/0703146v2]

Koyama, K., et al. 2007, PASJ, 59, 23

Kubo, H., Takahashi, T., Madejski, G., Tashiro, M., Makino, F., Inoue, S., & Takahara, F. 1998, ApJ, 504, 693

Laor, A., Fiore, F., Elvis, M., et al. 1997, ApJ, 477, 93

Lawson, A. J., Turner, M. J. L., Williams, O. R., Stewart, G. C., & Saxton, R. D. 1992, MNRAS, 259, 743

Liu, Y., Jiang, D. R., & Gu, M. F. 2006, ApJ, 637, 669

Lockman, F. J., & Savage, B. D. 1995, ApJS, 97, 1

Lovelace, R. V. E., Ustyugova, G. V., & Koldova , A. V. 1999, *Active Galactic Nuclei and Related Phenomena*, IAU Symposium, 194, 208

Madejski, G., et al. 1999, ApJ, 521, 145

Makino, F., et al. 1989, ApJ, 347, L9

Malkan, M. A., & Moore, R. L. 1986, ApJ, 300, 216

Mirabel, I. F., & Rodriguez, L. F. 1999, ARA&A, 37, 409

Mitsuda, K., et al. 1984, PASJ, 36, 741

Mitsuda, K., et al. 2007, PASJ, 59, 1

Moderski, R., Sikora, & Błażejowski, M. 2003, A&A, 406, 855

Moderski, R., & Sikora, M. 2007, to appear in "The Central Engine of Active Galactic Nuclei", ed. L. C. Ho and J.-M. Wang (San Francisco: ASP), arXiv:astro-ph/0612342

Moderski, R., Sikora, M., Madejski, G. M., & Kamae, T. 2004, ApJ, 611, 770

Moderski, R., Sikora, M., Coppi, P. S., & Aharonian, F. 2005, MNRAS, 363, 954

Ott, M., Witzel, A., Quirrenbach, A., Krichbaum, T. P., Standke, K. J., Schalinski, C. J., & Hummel, C. A. 1994, A&A, 284, 331

Page, K. L., Reeves, J. N., O'Brien, P. T., & Turner, M. J. L. 2005, MNRAS, 364, 195

Pian, E. & Treves, A. 1993, ApJ, 416, 130

Piran, T. 2000, Physics Reports, 333, 529

Porquet, D., Reeves, J. N., O'Brien, P., & Brinkmann, W., 2004, A&A, 422, 85

Raiteri, C. M., Villata, M., Lanteri, L., Cavallone, M., & Sobrito, G. 1998, A&AS, 130, 495

Romanova, M. M., & Lovelace, R. V. E. 1992, A&A, 262, 26

Roming, P. W. A., et al. 2005, Space Sci. Rev., 120, 95

Sambruna, R., et al. 2006, ApJ, 646, 23

Sambruna, R., et al. 2007, ApJ, in press

Sault, R. J., Teuben, P. J., & Wright, M. C. H., 1995, Astronomical Data Analysis Software and Systems IV, 77, 433

Serlemitsos, P. J., et al. 2007, PASJ, 59, 9

Schlegel, D. J., Finkbeiner, D. P., & Davis. M. 1998, ApJ, 500, 525

Siebert, J., et al. 1996, MNRAS, 279, 1331

Sikora, M., Begelman, M. C., & Rees, M. J., 1994, ApJ, 421, 153

Sikora, M., Madejski, G. Moderski, R., & Poutanen, J. 1997, ApJ, 484, 108

Sikora, M. & Madejski, G. M. 2000, ApJ, 534, 109

Sikora, M., Błażejowski, M., Moderski, R., & Madejski, G. M. 2002, ApJ, 577, 78

Sikora, M., Begelman, M. C., Madejski, G. M., & Lasota, J.-P. 2005, ApJ, 625, 72

Singh, K. P., Shrader, C. R., & George, I. M. 1997, ApJ, 365, 455

Sokolov, A., & Marscher, A.P. 2005, ApJ, 629, 52

Spada, M., Panaitescu, A., & Meszaros, P. 2000, ApJ, 537, 824

Stawarz, Ł., Cheung, C. C., Harris, D. E., & Ostrowski, M. 2007, ApJ, 662, 213

Stetson P. B. 1988, PASP, 99, 191

Tagliaferri, G., et al. 2000, A&A, 354, 431

Takahashi, T., et al. 2007, PASJ, 59, 35

Tanihata, C., et al. 2000, ApJ, 543, 124

Tanihata, C., Takahashi, T., Kataoka, J., & Madejski, G. M. 2003, ApJ, 584, 153

Tavecchio, F., et al. 2000, ApJ, 543, 535

Tavecchio, F., Maraschi, L., Ghisellini, G., Kataoka, J., Foschini, L., Sambruna, R. M., & Tagliaferri, G. 2007, ApJ, 665, 980

Tanner, A. M., Bechtold, J., Walker, C. E., Black, J. H., & Cutri, R. M. 1996, AJ, 112, 62

Tingay, S. J., Jauncey, D. L., King, E. A., Tzioumis, A. K., Lovell, J. E. J., & Edwards, P. G. 2003, PASJ, 55, 351

Tosti, G., Pascolini, S., & Fiorucci, M. 1996, PASP, 108, 706

Tosti, G., et al. 2004, Proc. SPIE, 5492, 689

Uchiyama, Y., et al. 2005, ApJ, 631, L113

Urry, C. M., & Padovani, P. 1995, PASP, 107, 803

Verkhodanov, O. V., Trushkin, S. A., Andernach, H., & Chernenkov, V. N. 1997, Astronomical Data Analysis Software and Systems VI, 125, 322

Villata M., et al. 1997, A&AS, 121, 119

Walter, R., & Fink, H. H. 1993, A&A, 274, 105

Wardle, J. F. C., Homan, D. C., Ojha, R., & Roberts, D. H. 1998, Nature, 395, 457

Wardle, J. F. C., Homan, D. C., Cheung, C. C., Roberts, D. H. 2005, in ASP Conf. Ser. 340, Future Directions in High Resolution Astronomy: The 10th Anniversary of the VLBA, ed. J. Romney, & M. Reid (San Frqancisco, ASP) 67

Williams, O. R., et al. 1992, ApJ, 389, 157

Zerbi, F. M., et al. 2004, Proc. SPIE, 5492, 1590

Zdziarski, A. A., Poutanen, J., & Johnson, W. N. 2000, ApJ, 542, 703

Table 1: 2006 *Suzaku*/*Swift* observation log of PKS 1510−089.

Instr start (UT)	stop (UT)	Exposure (ks)	Exposure (ks)
Suzaku		XIS	HXD
Aug 02 09:31	Aug 05 06:06	119.2	93.4
Swift		XRT	UVOT (v/b/u/uvw1/uvm2/uvw2)
Aug 04 14:09	Aug 04 16:10	2.6	0.10/0.13/0.13/0.27/0.11/0.55
Aug 05 01:10	Aug 05 04:35	2.1	0.09/0.09/0.09/0.17/0.23/0.35
Aug 08 05:07	Aug 08 14:54	2.2	0.07/0.07/0.07/0.14/0.16/0.27
Aug 09 04:49	Aug 09 14:31	1.6	0.07/0.07/0.07/0.14/0.14/0.28
Aug 10 09:47	Aug 10 16:13	0.5	0.05/0.05/0.05/0.12/0.11/0.21
Aug 11 00:15	Aug 11 22:51	4.3	0.14/0.14/0.14/0.29/0.37/0.58
Aug 18 00:57	Aug 18 23:30	3.2	0.13/0.13/0.13/0.27/0.25/0.54
Aug 19 01:02	Aug 19 07:37	2.6	0.11/0.11/0.11/0.22/0.28/0.46
Aug 20 02:46	Aug 20 09:20	2.2	0.09/0.09/0.09/0.18/0.21/0.37
Aug 21 20:32	Aug 22 23:55	3.0	0.13/0.13/0.13/0.25/0.35/0.52

Table 2: Optical observation log of PKS 1510−089.

Instr	Filter	start (UT)	stop (UT)	exp. [s]	Magnitude[a]
REM	V	2006 Aug 20 23:14:21	2006 Aug 21 00:00:52	3000	16.88 ±0.02[b]
REM	R	2006 Aug 19 23:13:21	2006 Aug 19 23:59:53	3000	16.10 ±0.01
REM	I	2006 Aug 21 00:06:22	2006 Aug 21 00:52:54	3000	16.10 ±0.01
Heidelberg	B	2006 Aug 01 20:25:12	2006 Aug 01 21:19:51	480	16.95 ±0.08
Heidelberg	R	2006 Aug 01 20:30:22	2006 Aug 01 21:24:23	480	16.15 ±0.05
Heidelberg	I	2006 Aug 01 20:35:09	2006 Aug 01 21:29:14	360	15.90 ±0.20

[a]Observed magnitude for each observation using specific filters (Galactic extinction not corrected). [b]: On August 19th PKS 1510−089 showed a very fast rise ($\Delta m_{\rm R} \simeq 0.6$) in less than one hour.

Table 3: Radio observation log of PKS 1510−089.

Instr	Frequency [GHz]	Observation Time	Flux density [Jy][a]
RATAN	1.0	2006 Aug 9 − Aug 23	1.88±0.07[b]
RATAN	2.3	2006 Aug 9 − Aug 23	2.01±0.05[b]
RATAN	4.8	2006 Aug 9 − Aug 23	2.08±0.03[b]
RATAN	7.7	2006 Aug 9 − Aug 23	2.09±0.04[b]
RATAN	11.1	2006 Aug 9 − Aug 23	2.05±0.21[b]
RATAN	21.7	2006 Aug 9 − Aug 23	1.68±0.08[b]
ATCA	1.4	2006 Jul 11	1.93±0.11
ATCA	2.3	2006 Jul 11	1.83±0.10
ATCA	4.8	2006 Jul 11	1.85±0.09
ATCA	8.6	2006 Jul 11	1.97±0.10
ATCA	1.4	2006 Aug 4	1.85±0.14
ATCA	2.4	2006 Aug 4	1.84±0.10
ATCA	4.8	2006 Aug 4	2.02±0.10
ATCA	8.6	2006 Aug 4	2.12±0.11
ATCA	18.5	2006 Aug 4	2.08±0.11
ATCA	19.5	2006 Aug 4	2.11±0.12

[a]The flux density errors presented do not include the error of the absolute radio flux density scale. See its estimate in Baars et al. (1977) and Ott et al. (1994).

[b]RATAN flux densities averaged over the period August 9–23, 2006.

Table 4: Results of the spectral fits to the 0.3−50 keV *Suzaku* spectrum with different models.

Model[a]	$N_{\rm H}$[b]	$\Gamma_{\rm high}$[c]	$\Gamma_{\rm low}$[d]	kT[e]	$F_{0.5-10\,{\rm keV}}$[f]	$F_{2-10\,{\rm keV}}$[f]	$F_{10-50\,{\rm keV}}$[f]	χ^2/d.o.f
PL	7.88	1.30±0.01	...	...	14.1±0.1	10.8±0.1	33.7±0.4	705/585
PL+PL	7.88	1.19±0.02	2.76±0.15	...	14.4±0.1	11.1±0.1	39.7±0.5	536/583
PL+BB	7.88	1.24±0.01	...	0.16±0.02	14.2±0.1	11.1±0.1	38.3±0.4	519/583
PL+DB	7.88	1.23±0.01	...	0.23±0.02	14.4±0.1	11.1±0.1	38.2±0.4	515/583

[a]Spectral fitting models. PL: power-law function, PL+PL: double power-law functions, PL+BB: power-law + blackbody model, PL+DB: power-law + disk blackbody model.

[b]Galactic absorption column density in units of 10^{20} cm^{-2}.

[c]Differential spectral photon index.

[d]Differential spectral photon index at low energy X-ray band, when fitted with a double power-law functions.

[e]Temperature at inner disk radius in keV, fitted with disk blackbody model by Mitsuda et al. (1984).

[f]Flux in units of 10^{-12} erg cm^{-2} s^{-1}.

Table 5: Correction factors for the Galactic extinction in UV and optical filters.

Filter	λ [nm][a]	$a^\dagger$	$b^\dagger$	$A_\lambda^\dagger$	$C_{\rm cor}$[b]
I	800	0.7816	−0.5707	0.18	1.18
R	650	0.9148	−0.2707	0.25	1.26
v	547	1.0015	0.0126	0.30	1.32
b	439	0.9994	1.0171	0.40	1.45
u	346	0.9226	2.1019	0.48	1.56
uvw1	260	0.4346	5.3286	0.65	1.82
uvm2	249	0.3494	6.1427	0.70	1.91
uvw2	193	−0.0581	8.4402	0.80	2.09

[a]Center wavelength for each optical/UV filters.

[†]Parameters for calculating Galactic extinction for optical and UV filters, calculated according to the prescription in Cardelli, Clayton & Mathis (1989). The Galactic reddening was taken from Schlegel, Finkbeiner, & Davis (1998).

[b]Correction factor for Galactic extinction.

Table 6: The input parameters for modelling of the non-thermal emission of PKS 1510−089.

Parameter	Model A	Model B
minimum electron Lorentz factor $\gamma_{\rm min}$	1	1
break electron Lorentz factor $\gamma_{\rm br}$	100	150
maximum electron Lorentz factor $\gamma_{\rm max}$	10^5	10^5
low-energy electron spectral index p	1.35	1.35
high-energy electron spectral index q	3.25	3.25
normalization of the injection function K_e	$0.9 \times 10^{47}\,{\rm s}^{-1}$	$1.7 \times 10^{47}\,{\rm s}^{-1}$
bulk Lorentz factor of the emitting plasma $\Gamma_{\rm jet}$	20	20
jet opening angle $\theta_{\rm jet}$	0.05 rad	0.02 rad
jet viewing angle $\theta_{\rm obs}$	0.05 rad	0.05 rad
scale of the emission zone $r_{\rm sh}$	10^{18} cm	10^{18} cm
jet magnetic field intensity B	1.3 G	0.86 G
scale of the dominant external photon field $r_{\rm ext}$	3.0×10^{18} cm	3.0×10^{18} cm
luminosity of the external photon field $L_{\rm ext}$	$3.7 \times 10^{45}\,{\rm erg\,s}^{-1}$	$3.7 \times 10^{45}\,{\rm erg\,s}^{-1}$
photon energy of the external photon field $h\nu_{\rm ext}$	0.2 eV	0.2 eV
total energy of radiating electrons E_e	1.3×10^{48} erg	3.1×10^{48} erg
comoving electron energy density u'_e	$0.015\,{\rm erg\,cm}^{-3}$	$0.022\,{\rm erg\,cm}^{-3}$
equipartition magnetic field $B_{\rm eq}$	0.6 G	2.4 G
kinetic luminosity of radiating electrons L_e	$1.4 \times 10^{45}\,{\rm erg\,s}^{-1}$	$3.3 \times 10^{45}\,{\rm erg\,s}^{-1}$
soft X-ray excess	bulk-Compton	SSC

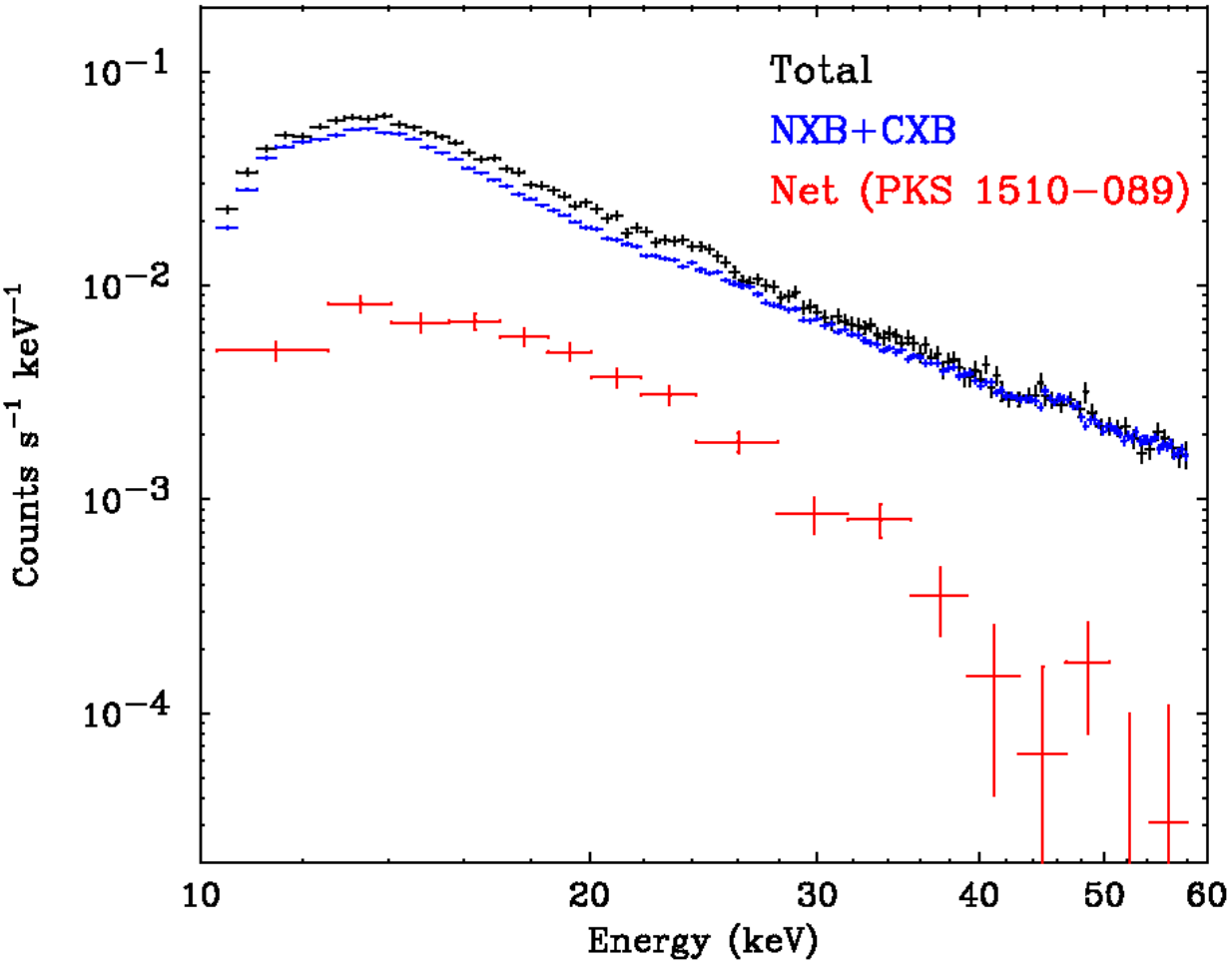

Fig. 1.— The combined HXD/PIN spectra for the *Suzaku* observation of PKS 1510−089 over the whole HXD/PIN energy bandpass (10−60 keV). *Black* (upper): source plus background spectrum, *blue* (middle): sum of the non–X-ray background and CXB, and *red* (bottom): for the net source spectrum.

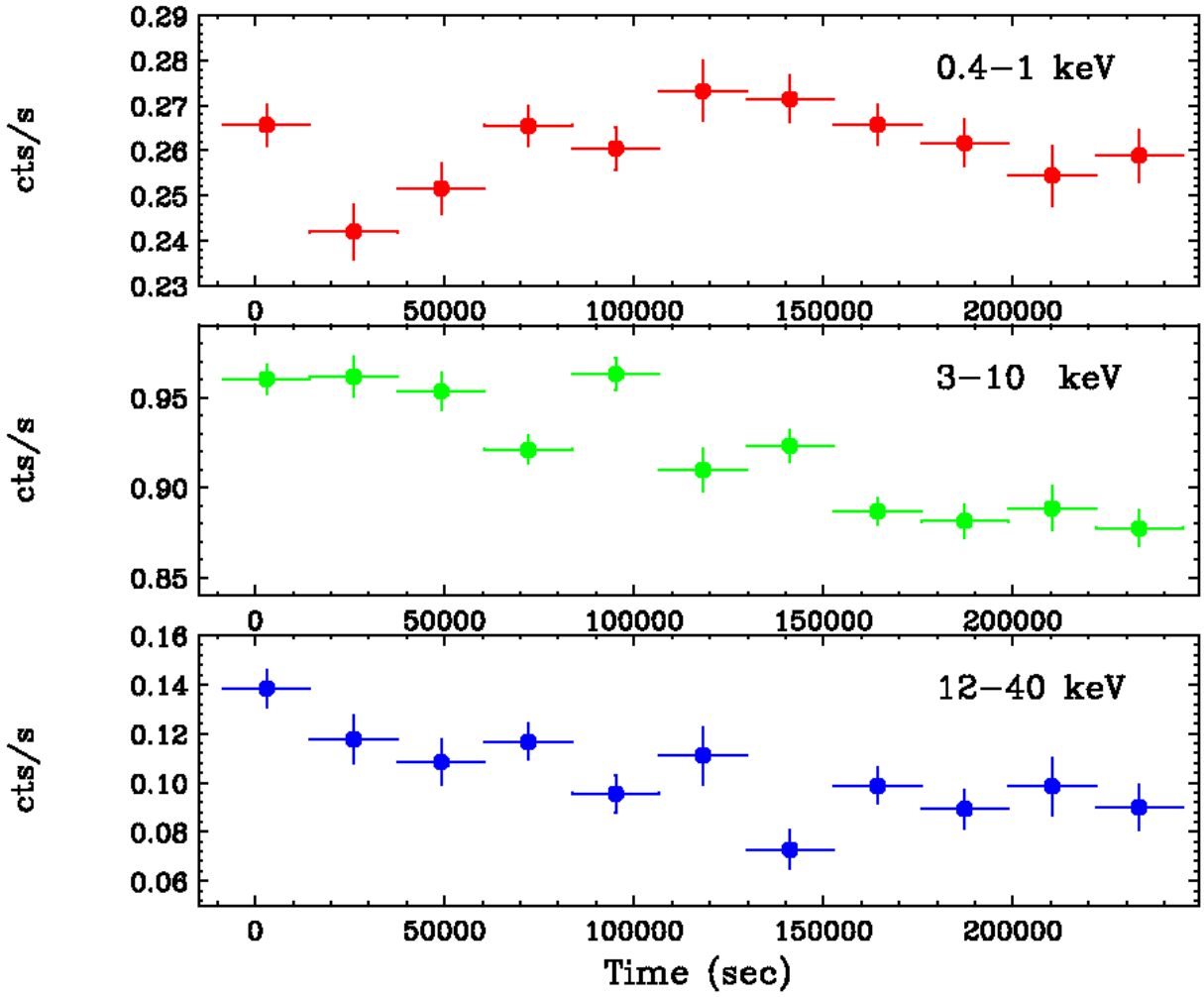

Fig. 2.— The overall variability of PKS 1510−089 observed with *Suzaku* in 2006 August. *upper panel*: 0.4−1 keV (XIS 0−3 summed), *middle panel*: 3−10 keV(XIS 0−3 summed), and *lower panel*: 12−40 keV (HXD/PIN W0−3 summed).

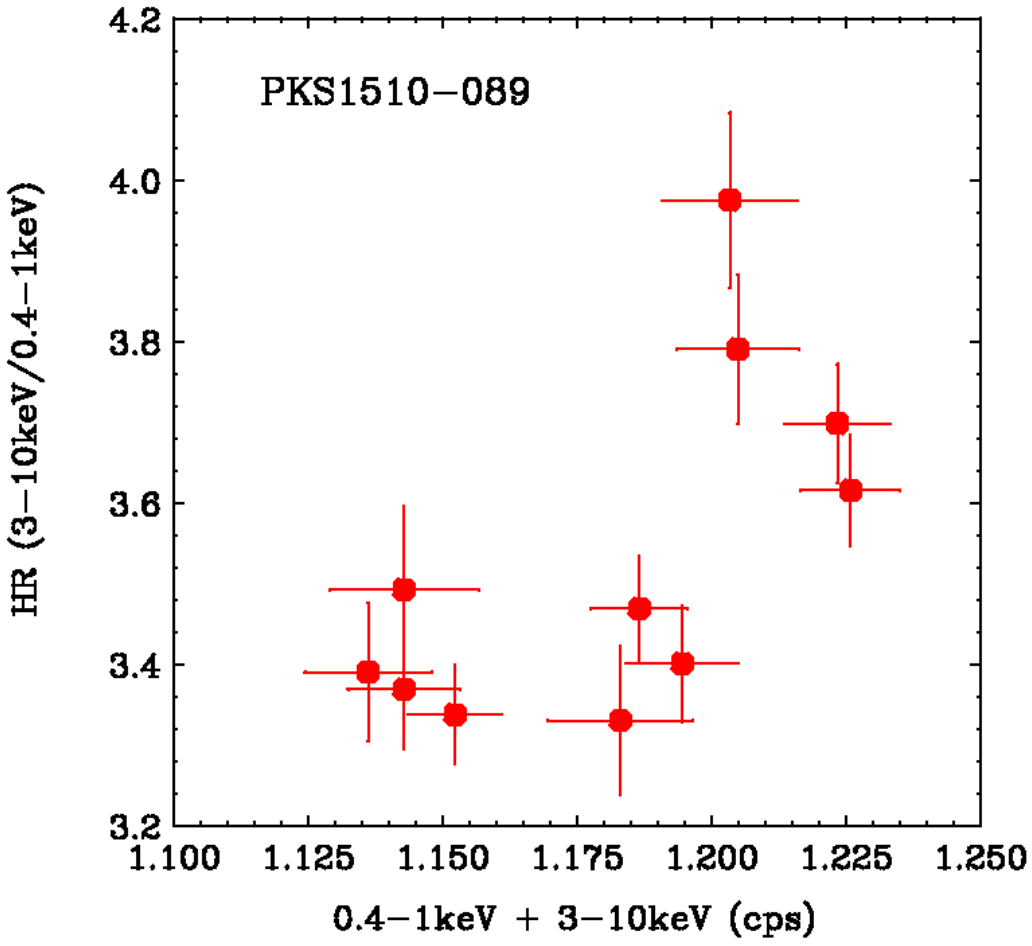

Fig. 3.— Changes in the hardness ratio between 0.4−1 keV and 3−10 keV. The hardness is defined as the 3−10 keV count rate divided by the 0.4−1 keV count rate (XIS 0−3 summed).

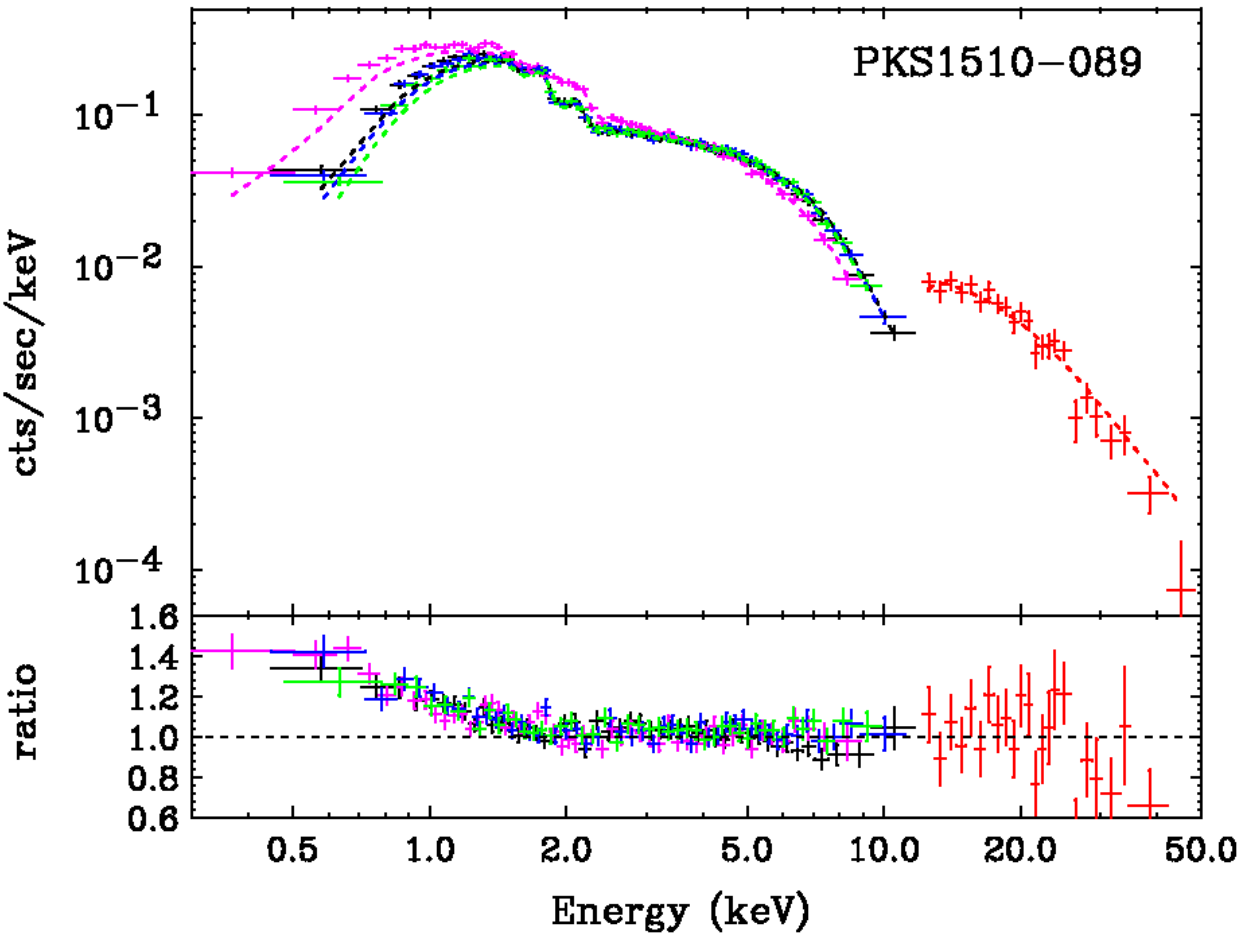

Fig. 4.— *upper panel*: The broadband (0.3−50 keV; XIS0−3 + HXD/PIN) *Suzaku* spectrum of PKS 1510−089. The upper panel shows the data, plotted against an absorbed power-law model of photon index $\Gamma = 1.2$ and a column density 7.88×10^{20} cm^{-2}, fitted over the 2−50 keV band. The *lower panel* shows the data/model ratio residuals to this power-law fit. Deviations due to excess soft emission are clearly seen.

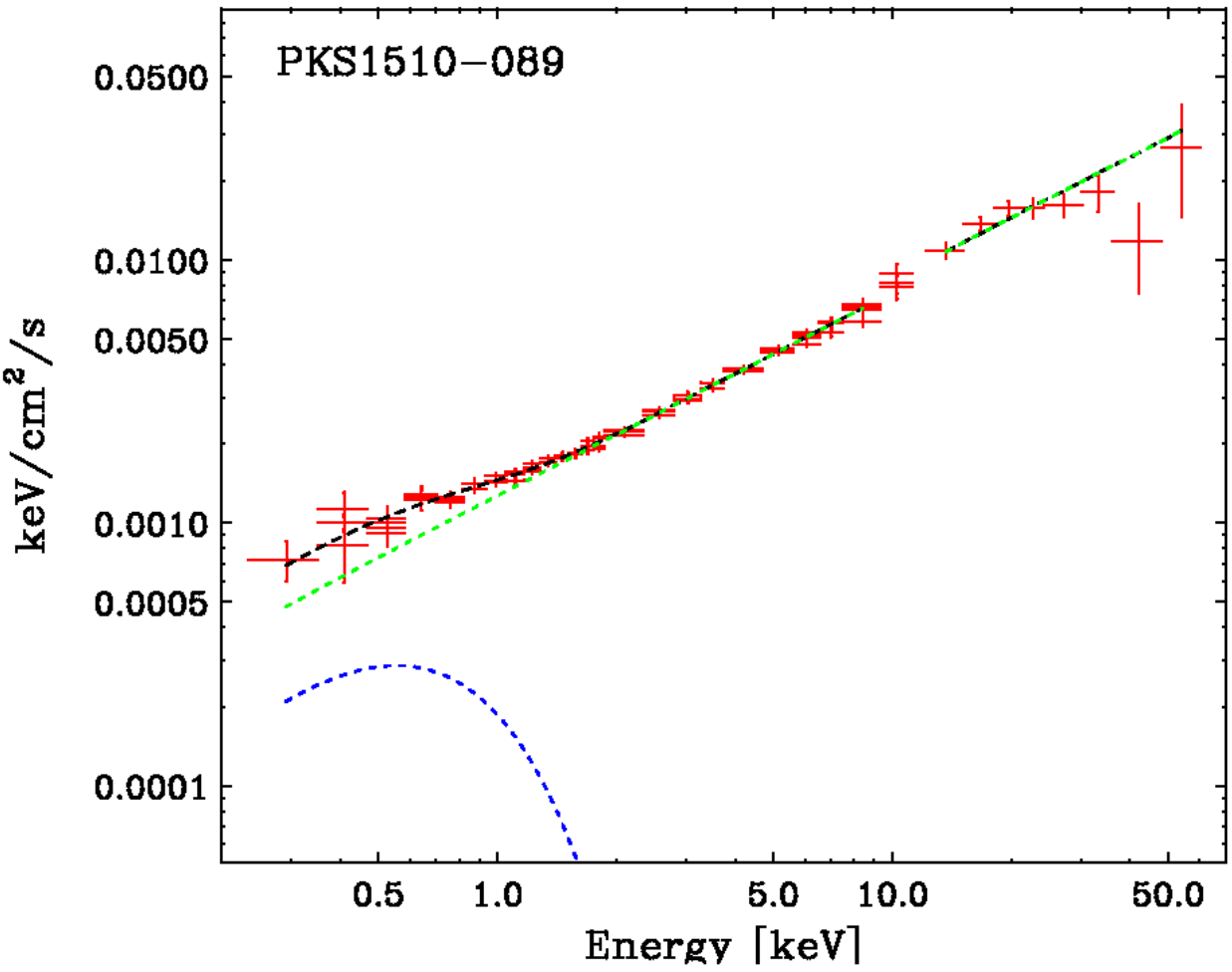

Fig. 5.— The unfolded *Suzaku* spectrum between 0.3 and 50 keV (in νF_ν space), plotted against the best-fit model composed of an absorbed power-law ($\Gamma = 1.2$: green) plus disk black body emission (kT = 0.2 keV: blue). The black line shows the sum of the model components.

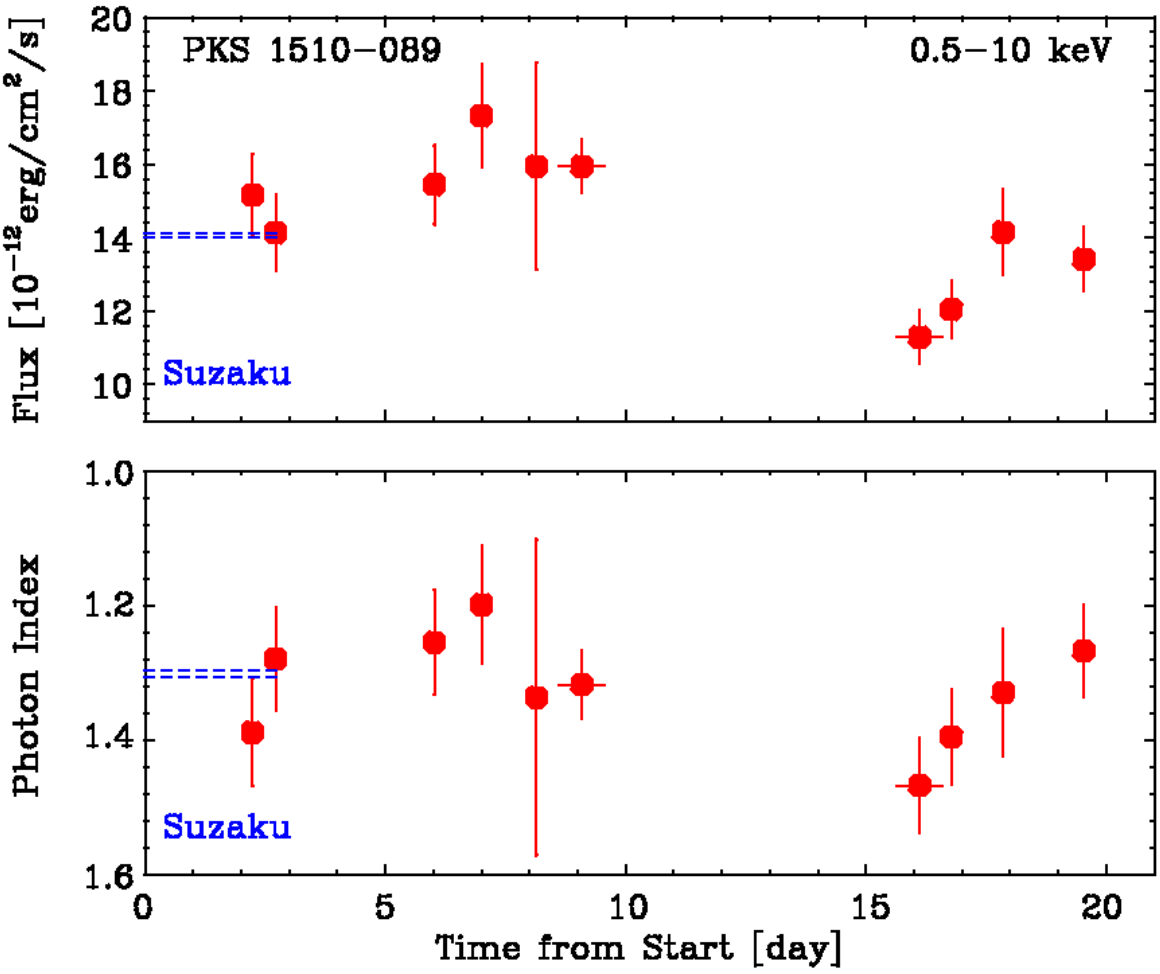

Fig. 6.— Spectral variability of the *Swift*/XRT data during the 2006 August campaign. The observation time is measured from the start of the *Suzaku* observation, i.e., 2006 August 2, 09:31:29 UT, and the blue dashes show the best-fit parameters determined by *Suzaku*. *upper panel*: changes in the 0.5−10 keV fluxes. Absorption corrected. *lower panel*: changes in the power-law photon index.

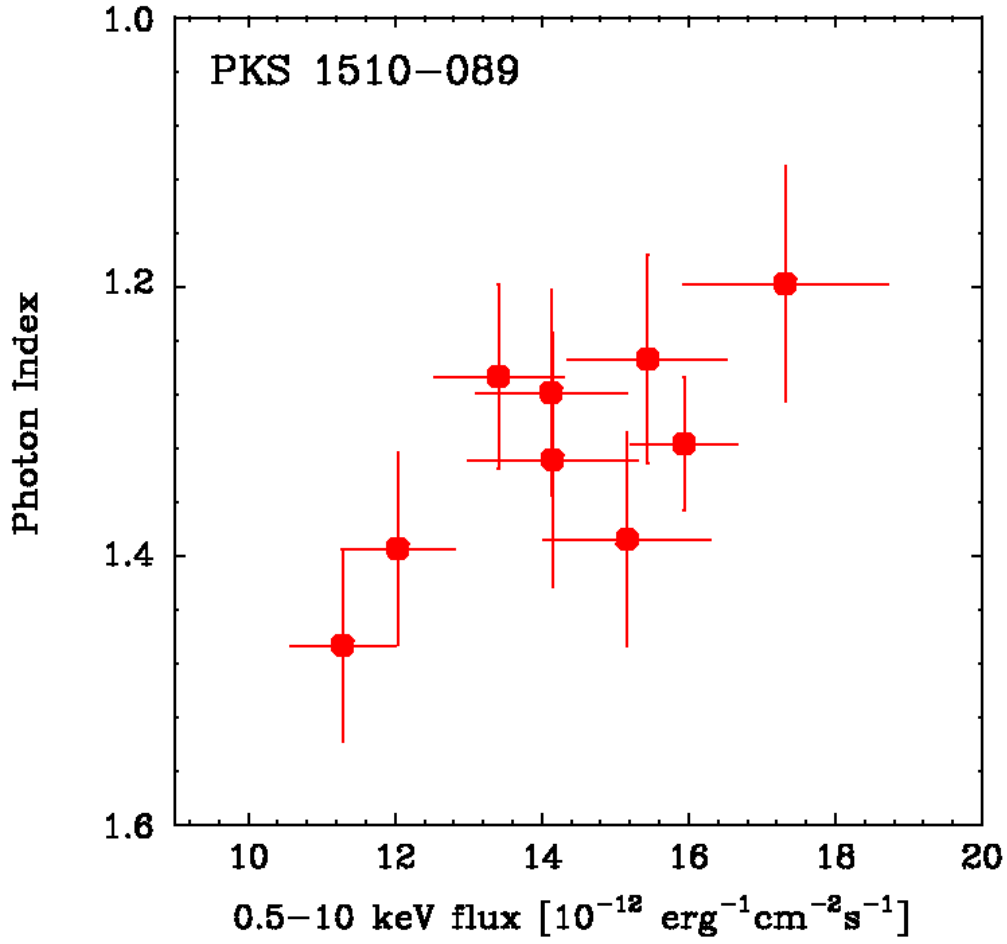

Fig. 7.— Correlation of the 0.5−10 keV flux versus photon index measured by the *Swift*/XRT. Data for observation #5 has been ignored in this plot simply due to the large uncertainties (see error bars in Figure 6).

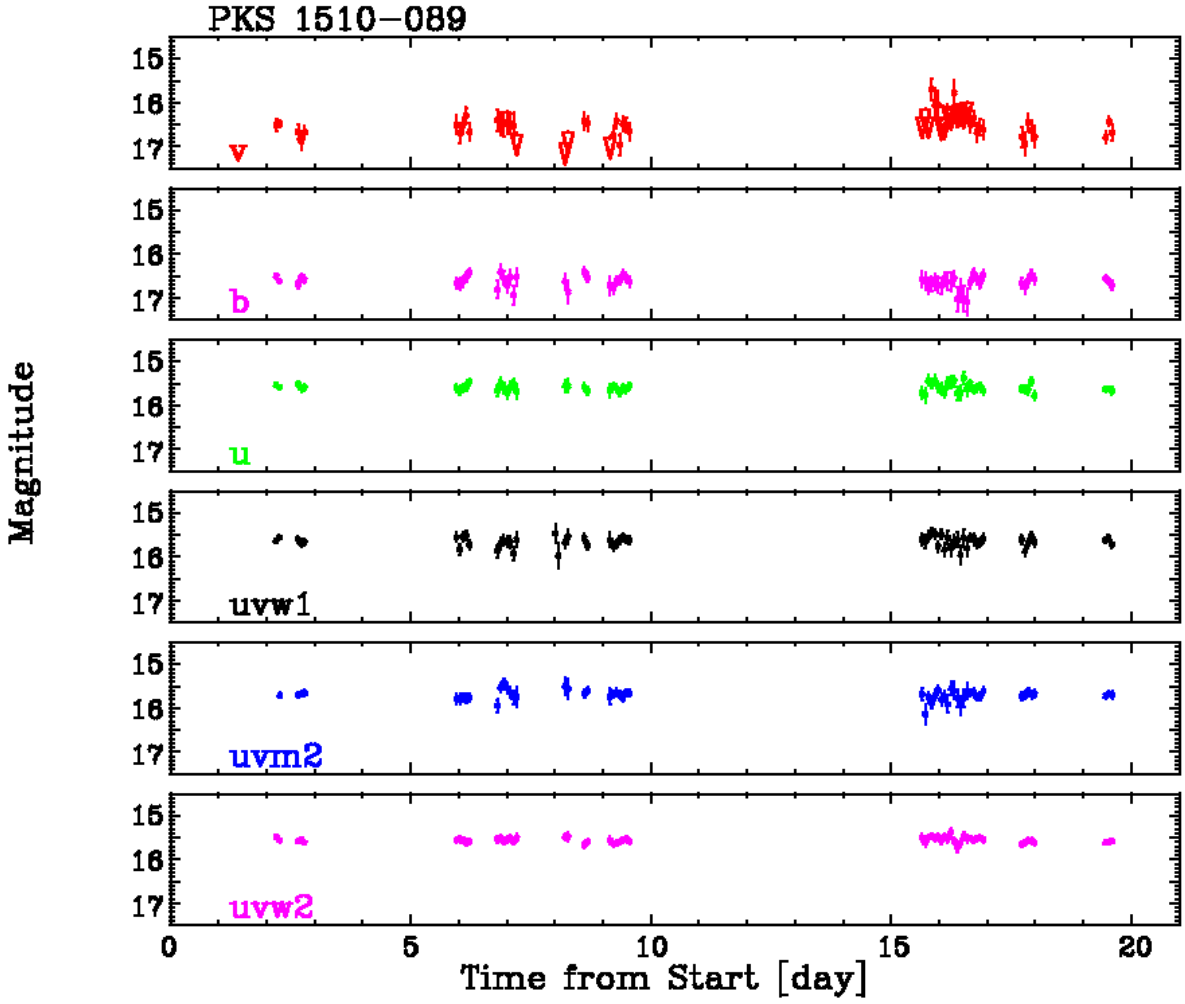

Fig. 8.— The overall variability of the *Swift*/UVOT data during the 2006 August campaign. From top to bottom; v-band, b-band, u-band, uvw1-band, uvm2-band, and uvw2-band. For more details about UVOT filters and their wavelength properties, see Poole et al., in preparation, and http://swift.gsfc.nasa.gov/docs/swift/about_swift/uvot_desc.html.

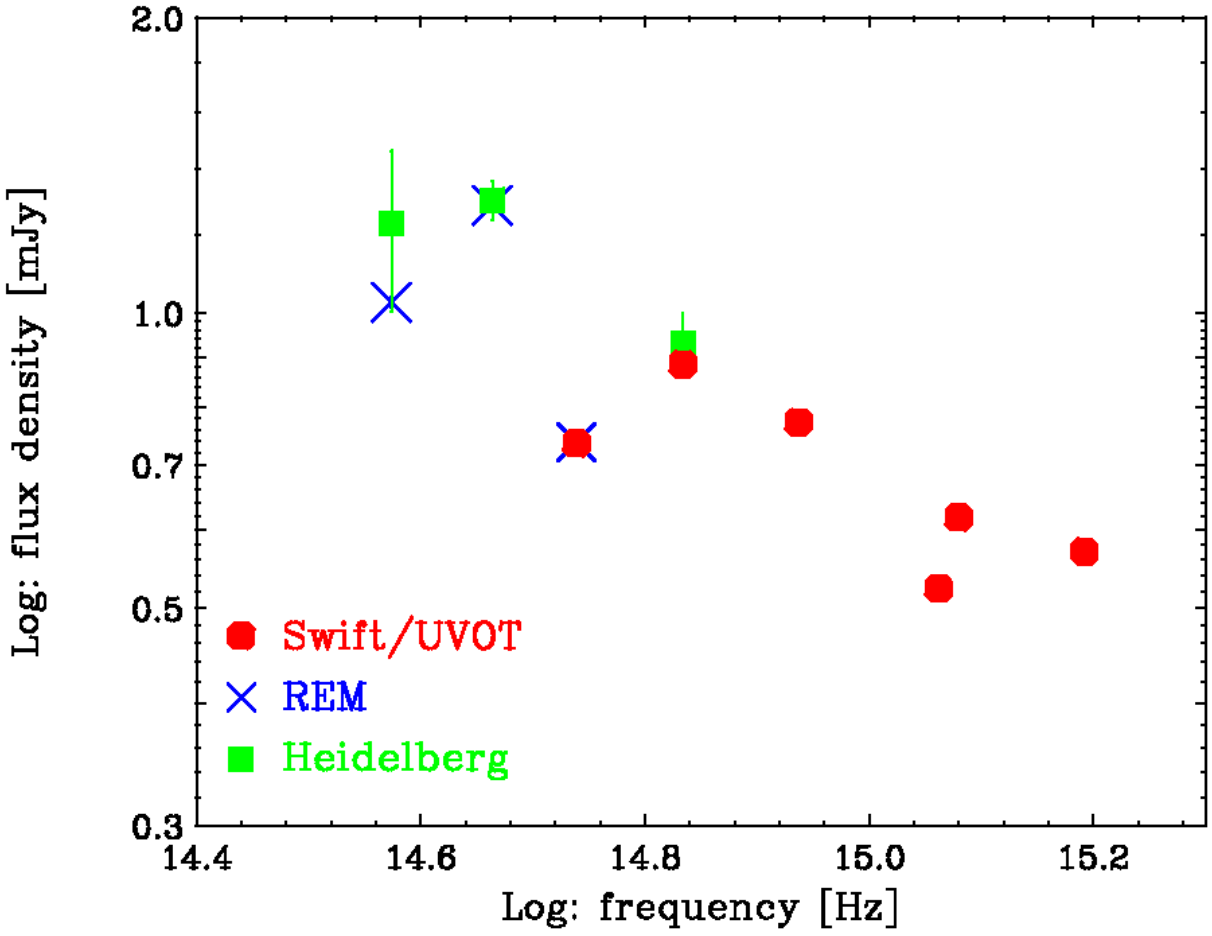

Fig. 9.— Combined optical spectrum of PKS 1510−089 taken during the 2006 August campaign. Data are corrected for the Galactic extinction using relations in Cardelli, Clayton & Mathis (1989). Note the perfect consistency between *Swift*/UVOT, REM and Heidelberg telescopes.

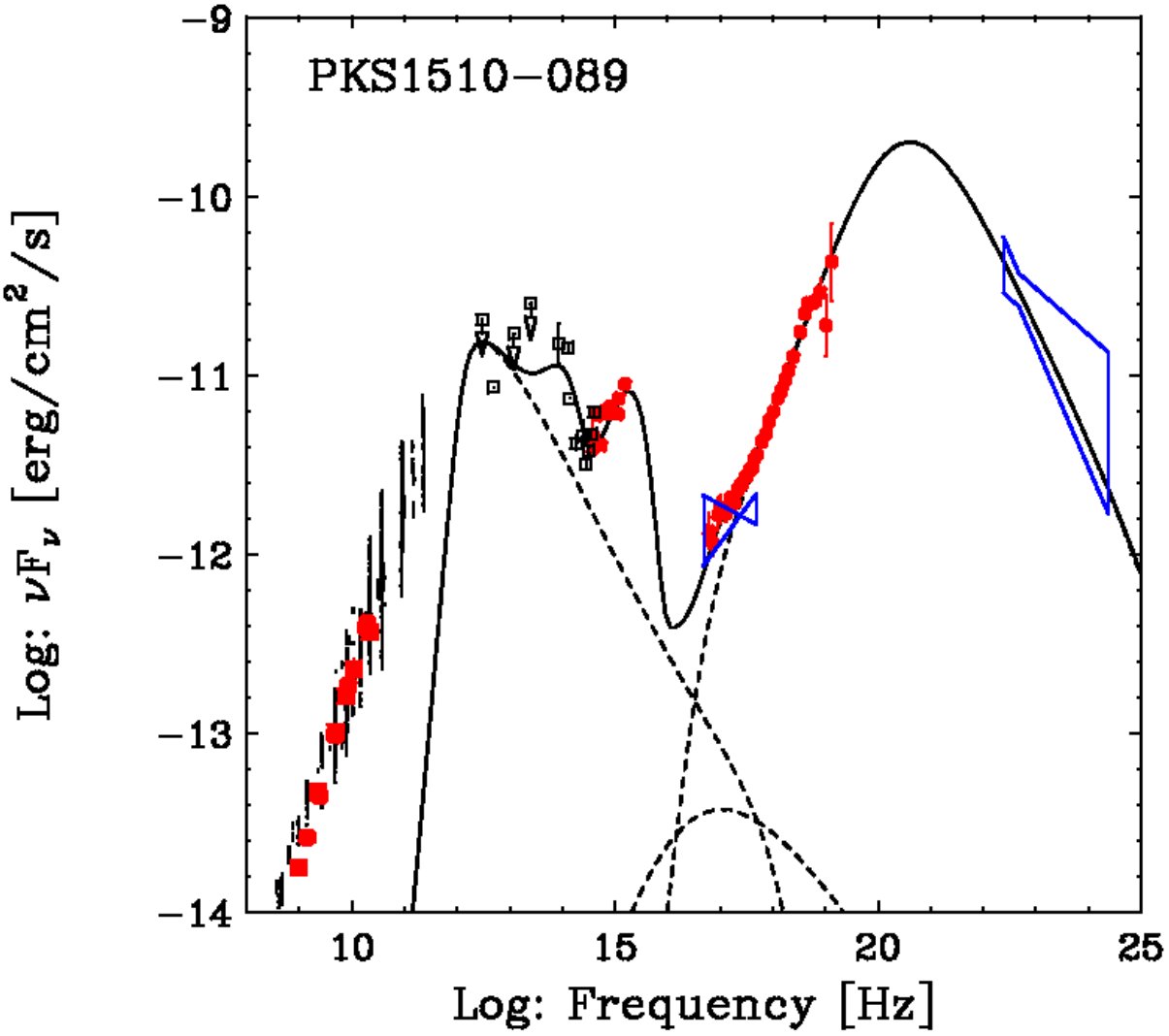

Fig. 10.— Overall SED of PKS 1510−089 constructed with multiband data obtained during this campaign (*filled circles*): radio (RATAN-600 and ATCA), optical (*Swift* UVOT, REM and Heidelberg), X-ray (*Suzaku*). Historical data taken from radio (NED and CATS), IR (*IRAS*; Tanner et al. 1996) optical (NED), soft X-ray (*ROSAT*; left bow-tie from Siebert et al. 1996) and γ-ray (EGRET; right bow-tie from Hartman et al. 1999) databases are also plotted as black points. The thick line shows the spectrum calculated using the jet emission model described in the text, as a sum of various emission components (dotted lines; synchrotron, SSC, and ERC(IR); from left to right). The input parameters for this model are: $\gamma_{\rm min} = 1$, $\gamma_{\rm br} = 100$, $\gamma_{\rm max} = 10^5$, $p = 1.35$, $q = 3.25$, $K_e = 0.9{\times}10^{47}$ s^{-1}, $\Gamma_{\rm jet} = 20$, $\theta_{\rm jet} = 0.05$ rd, $\theta_{\rm obs} = 0.05$ rd, $r_{\rm sh} = 10^{18}$ cm, $B = 1.3$ G, $r_{\rm ext} = 3.0{\times}10^{18}$ cm, $L_{\rm ext} = 3.7{\times}10^{45}$ erg s^{-1}, and $h\nu_{\rm ext} = 0.2$ eV. See Moderski, Sikora & Błażejowski (2003) for the definition of the input parameters.

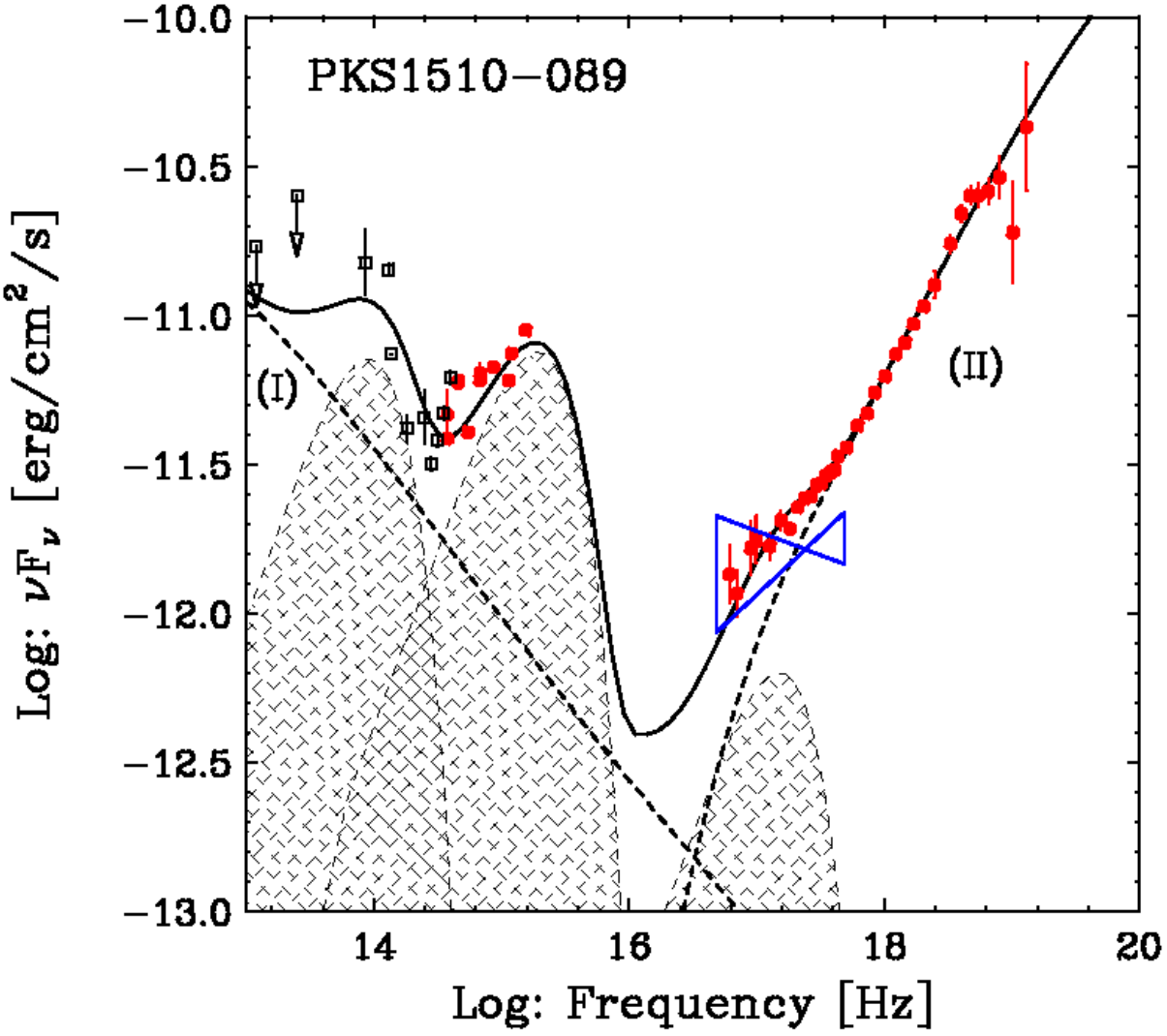

Fig. 11.— A close-up of the PKS 1510−089 SED model presented in Figure 10 between the optical and the X-ray bands. Here are added three blackbody-type humps: the left hump mimics an excess emission from the dusty torus as suggested by *IRAS* (Tanner et al. 1996), whereas the middle hump mimics the blue bump expected for this source from combined *Swift*/UVOT, REM, and Heidelberg data. The right hump shows the best fit blackbody-type emission of $kT \simeq 0.2\,\mathrm{keV}$ from the *Suzaku* fitting (Table 4). Dotted lines show (I) the Synchrotron and (II) the ERC components, respectively.A thick line shows sum of all the model components.

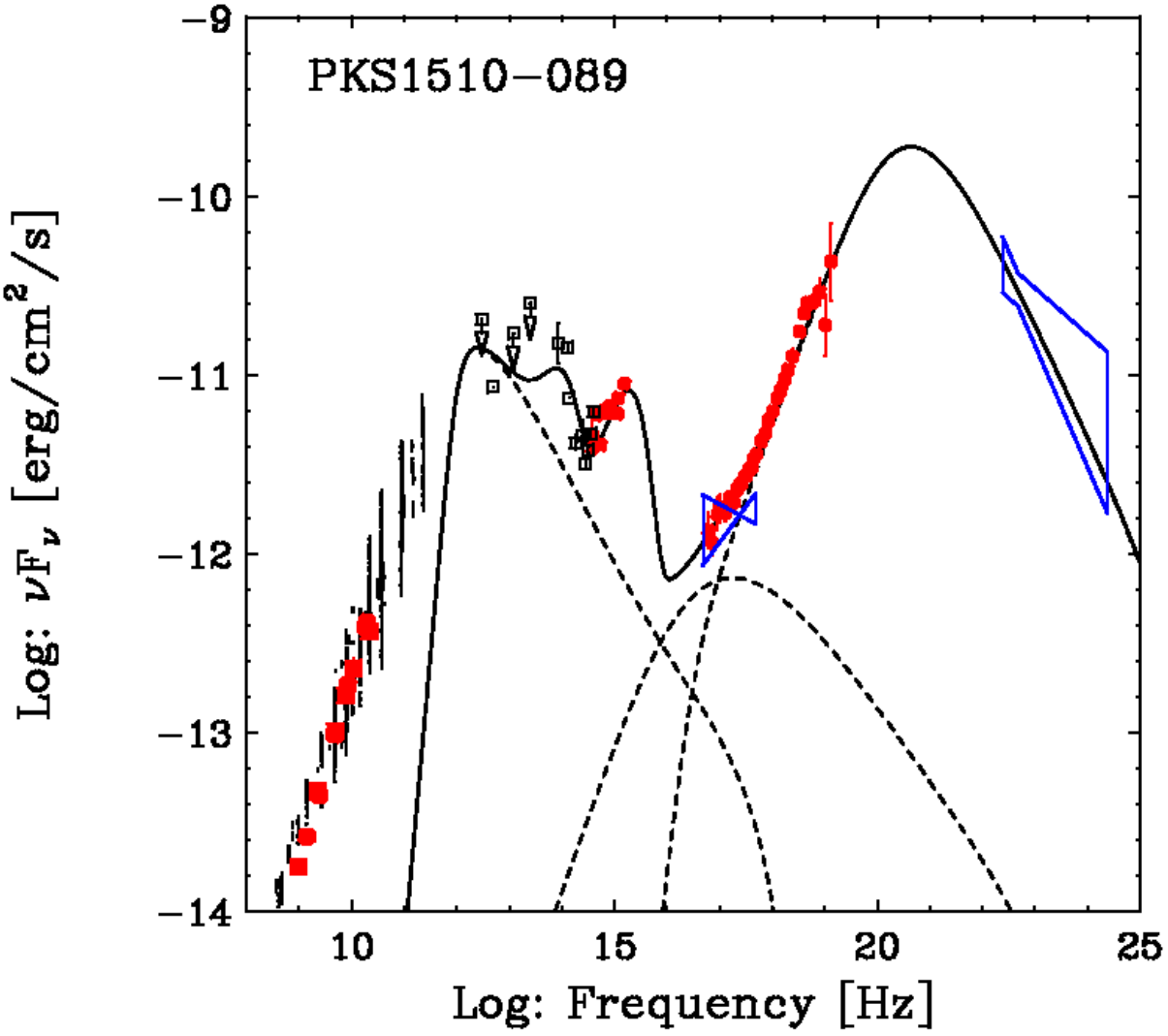

Fig. 12.— Same as Figure 10, but with somewhat different input model parameters: $\gamma_{\rm min} = 1$, $\gamma_{\rm br} = 150$, $\gamma_{\rm max} = 10^5$, $p = 1.35$, $q = 3.25$, $K_e = 1.7{\times}10^{47}$ s^{-1}, $\Gamma_{\rm jet} = 20$, $\theta_{\rm jet} = 0.02$ rd, $\theta_{\rm obs} = 0.05$ rd, $r_{\rm sh} = 10^{18}$ cm, $B = 0.86$ G, $r_{\rm ext} = 3.0{\times}10^{18}$ cm, $L_{\rm ext} = 3.7{\times}10^{45}$ erg s^{-1}, and $h\nu_{\rm ext} = 0.2$ eV.

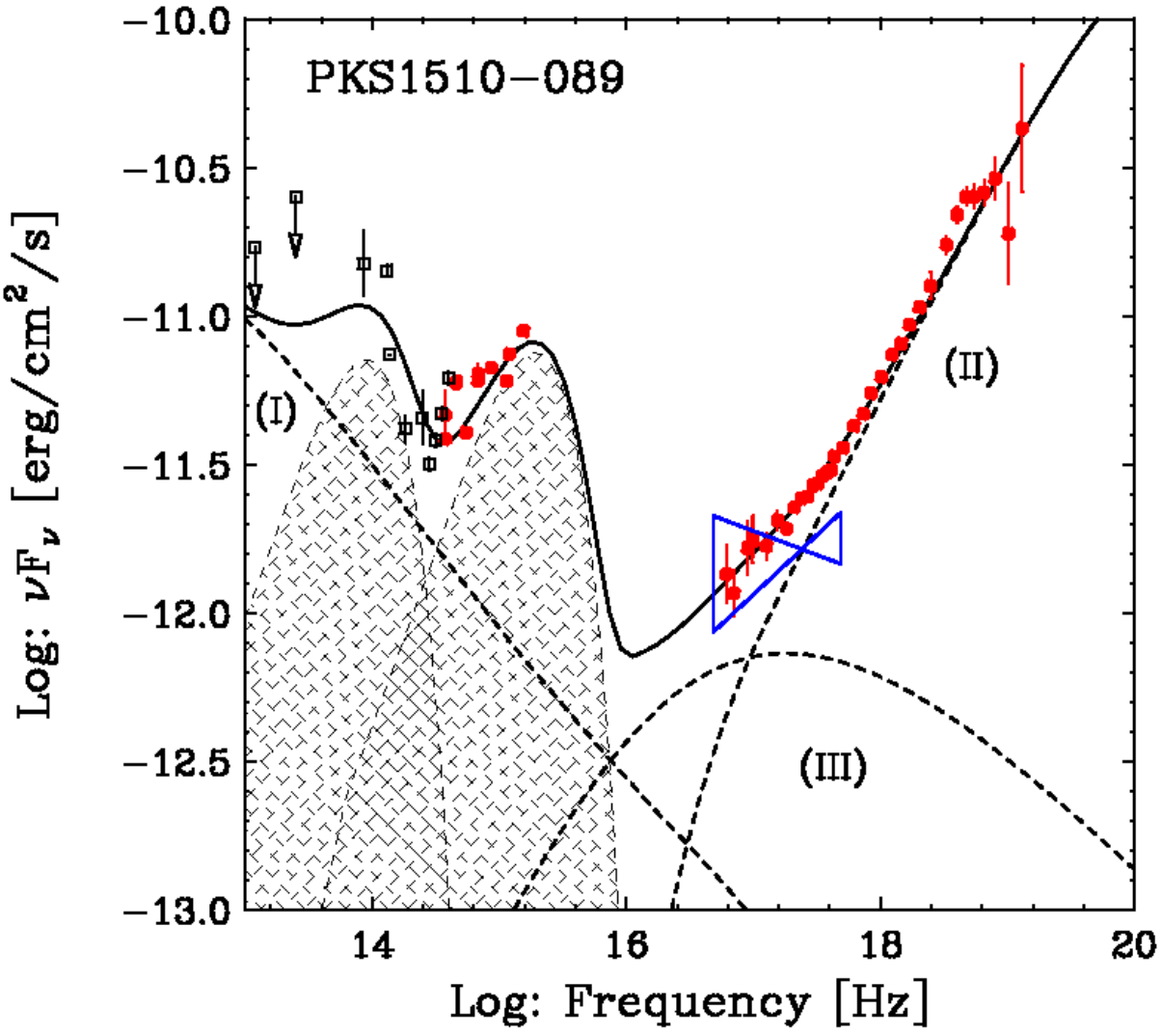

Fig. 13.— A close-up of the PKS 1510−089 SED model presented in Figure 12 between the optical and the X-ray bands. The left hump mimics an excess emission from the dusty torus as suggested by *IRAS* (Tanner et al. 1996), whereas the right bump expected for this source from combined *Swift*/UVOT, REM, and Heidelberg data. Dotted lines show: (I) the Synchrotron; (II) the ERC; and (III) the SSC components, respectively. A thick line shows sum of all the model components.